Project 019 Development of Aviation Air Quality Tools for Airshed-Specific Impact Assessment: Air Quality Modeling

University of North Carolina at Chapel Hill

Project Lead Investigator

Saravanan Arunachalam, Ph.D.
Research Professor
Institute for the Environment
University of North Carolina at Chapel Hill
100 Europa Drive, Suite 490
Chapel Hill, NC 27517
919-966-2126
sarav@email.unc.edu

University Participants

University of North Carolina at Chapel Hill (UNC)

- PI: Saravanan Arunachalam, research professor and deputy director
- FAA Award Number: 13-C-AJFE-UNC Amendments 1-18
- Period of Performance: October 1, 2021 to September 30, 2022
- Tasks: Development of new aircraft dispersion model (ADM)

Project Funding Level

FAA provided $650,000 in funding. EU-AVIATOR provided matching cost-share.

Investigation Team

Saravanan Arunachalam (PI)
Chowdhury Moniruzzaman (postdoctoral fellow #1)
Gavendra Pandey (postdoctoral fellow #2)
Ramarao Mandavilli (postdoctoral fellow #3)
Christos Efstathiou (emissions modeler)
Praful Dodda (graduate student #1)
Hyeongseok "Darby" Kim (graduate student #2)
Brian Naess (GIS specialist)
Consultant: Dr. Akula Venkatram, University of California at Riverside

Project Overview

Aviation is predicted to grow steadily in upcoming years;[1] thus, a variety of aviation environmental policies will be required to meet emission reduction goals in aviation-related air quality and health impacts. Tools are needed to rapidly assess the implications of alternative policies for an evolving population and atmosphere. In the context of the International Civil Aviation Organization (ICAO)'s Committee on Aviation Environmental Protection (CAEP), additional approaches are required to determine the implications of global aviation emissions.

The overall objective of this project is to develop a new aircraft-specific dispersion model and continue the development and implementation of tools, both domestically and internationally, to allow for an assessment of year-to-year changes in significant health outcomes. These tools must be acceptable to the FAA (in the context of Destination 2025) and/or other

[1] Boeing Commercial Airplane Market Analysis, 2010.

decision-makers. More importantly, this new model must have the capability to address the 1-hour form of the NO_2 National Ambient Air Quality Standard (NAAQS) in the United States, as well as support National Environmental Policy Act (NEPA) and/or NAAQS analyses that may be needed by airports. The developed methods must also rapidly provide output in order to support a variety of "what if" analyses and other investigations. While the tools for use within and outside the United States need not be identical, several goals are desirable for both cases:

- Enable the assessment of premature mortality and morbidity risks due to aviation-attributable particulate matter (PM) having diameter up to 2.5 μm ($PM_{2.5}$), ozone, and other pollutants known to exert significant health impacts;
- Capture airport-specific health impacts at regional and local scales;
- Account for the impact of landing/take-off (LTO) versus non-LTO emissions, including a separation of effects;
- Allow for an assessment of a wide range of aircraft emission scenarios, including differential growth rates and emission indices;
- Account for changes in nonaviation emissions;
- Allow for assessments of sensitivity to meteorology;
- Provide domestic and global results;
- Include quantified uncertainties and differences with respect to Environmental Protection Agency (EPA) practices, which are to be minimized when scientifically appropriate; and
- Be computationally efficient such that tools can be used in time-sensitive rapid turnaround contexts and for uncertainty quantification.

During this period of performance, the University of North Carolina at Chapel Hill's Institute for the Environment (UNC-IE) team performed work on the two tasks below:

Task 1 - Develop and Evaluate a New Dispersion Model for Aircraft Sources

University of North Carolina at Chapel Hill

Objectives

The FAA's Aviation Environmental Design Tool (AEDT) is currently coupled with the U.S. EPA's AERMOD dispersion model for modeling aircraft sources and is the required regulatory model in the United States for modeling airport-level aircraft operations during LTO cycles.

Recent studies have shown several limitations in the use of AERMOD for modeling aircraft sources. The Airport Modeling Advisory Committee (AMAC) developed a series of recommendations in 2011 to improve modeling jet exhaust. Since then, Airport Cooperative Research Program (ACRP) project 02-08 developed a guidance for airport operators on conducting measurement and modeling for air quality at airports, published in ACRP Report 70 (Kim et al., 2012). This study conducted a measurement and modeling study at Washington Dulles International Airport (IAD). Since then, ACRP project 02-58 developed a final report ACRP Report 171 (Arunachalam et al., 2017a) for providing dispersion modeling guidance for airport operators for local air quality and health. This study applied four different dispersion models—AERMOD, CALPUFF, SCICHEM, and the U.K.'s ADMS-Airport—for the Los Angeles International Airport (LAX) and compared modeled predictions with high-resolution measurements taken during the Los Angeles Air Quality Source Apportionment Study (AQSAS). All of these reports identified several limitations with AERMOD and developed a series of recommendations for improving dispersion modeling of aircraft emissions for airport-level air quality.

UNC recently developed the C-AIRPORT dispersion model for application to LAX (Arunachalam et al., 2017b). Initially, C-AIRPORT was designed to be part of the C-TOOLS series of community-scale, web-based modeling systems. The objective of C-TOOLS was to create a web-based interface to model multiple source types for short-term or long-term pollutant concentration averages and perform various "what if" scenarios that assess the changes in air quality at local scales due to changes in inputs. C-AIRPORT used a line source–based approach to model aircraft sources, based upon the C-LINE modeling system (Barzyk et al., 2015), and preliminary evaluation of the algorithms against LAX AQSAS was conducted.

Under the previous year's funding, UNC completed development of a modeling framework that addresses known limitations from the above tasks and proposed a viable and suitable approach for modeling pollutants from aircraft sources. The primary objective of this plan was to demonstrate that a robust, improved pollutant dispersion model for aircraft can be developed for U.S. regulatory compliance purposes. The proposed new model will disperse pollutants from aircraft sources in a more

technically and scientifically advanced manner (compared with current AERMOD capabilities), with the ultimate goal of becoming a potential U.S. regulatory compliance tool, based on future discussions between FAA and EPA. This plan will include an itemized list of known limitations along with a corresponding proposed developmental approach with recommendations to address them.

As part of the proposed ASCENT research under this task, we will continue to implement the plan with specific focus on four broad areas, over a period of 2 years. We give a very high-level summary here, because the actual specifics of this implementation are described in previous documents and reports that were independently developed earlier.

Our approach is to ensure that the new model will be "robust" and based on the state-of-science on physical and chemical processes and the associated algorithms.

1) **Source Characterization**
   Existing approaches in AEDT/AERMOD treat aircraft sources as an area source segment. In ongoing work, we are moving away from that approach to treat aircraft sources as line segments, as described in Arunachalam et al. (2019). We are currently adapting new high-resolution aircraft movement data from a research version of AEDT for an airport for use in the new dispersion model last year. We will finalize the approach with a streamlined tool for data processing in the dispersion model, and this will be tested and verified for implementation in AEDT.
2) **Physical Processes**
   We will go beyond the initial implementation last year, with specific new focus on the following:
   i. Treatment of dispersion under low wind conditions and assessment of effects of atmospheric stability
   ii. Treatment of dry and wet deposition
   iii. Exploration of additional options for aircraft exhaust plume rise such as the fluid mechanical entrainment (FEM) model that was scoped out in the ACRP report 171, where four new options can be implemented and evaluated:
      a. An empirical model for plume rise and initial dispersion based on LIDAR (light detection and ranging) measurements at LAX (Wayson et al., 2004),
      b. An FEM based on the average ground roll speed along the runway,
      c. An FEM as a function of the ground roll speed or distance down the runway (i.e., a different plume rise for each AERMOD area source, which is a function of runway distance), and
      d. An FEM based both on distance and time as independent variables describing the plume.
   iv. Incorporation of aircraft downwash effects
   v. Treatment of complex terrain and building downwash
3) **Chemical Processes**
   - We will go beyond the initial implementation last year, with specific new focus on the following:
     i. Note that the 1-hr form of the NO_2 NAAQS is a critical issue for air quality around U.S. airports, with several modeling studies showing overestimates of these compared to observations. It is important that the new model performs adequately to capture this short-term form of the NO_2 NAAQS.
     ii. New detailed chemical mechanism for NO_2 including the generic reaction set (GRS) (Valencia et al., 2017; Venkatram et al., 1994) or other,
     iii. Condensed version of the aerosol treatment as included in CMAQ and SCICHEM and described in Chowdhury et al. (2015)
4) **Model Evaluation**
   - Ongoing model evaluation involved evaluating model predictions using only measurements from the LAX AQSAS for winter 2012. We will now look at developing and testing the model for other case studies, including the following:
     i. LAX AQSAS for summer 2012.
     ii. One of three airports (Copenhagen, Madrid, and Zurich) with measurements being undertaken as part of the EU-AVIATOR project (see https://aviatorproject.eu/). We will rely on the AVIATOR team to provide emissions inventories for the chosen airport. If emissions inventories are not directly available for use, we will obtain airport operations data for the campaign period and develop an inventory using AEDT.
     iii. New measurements from ASCENT 18 investigators at Boston Logan International Airport (BOS). *This is new collaboration that will help focus on both designing the monitoring campaign to assist in obtaining valuable data to characterize aircraft emissions impacts on air quality and*

developing the ADM, as well as in source attribution of the measured fields to the aircraft or other source types.

- Model evaluation will focus on the model's ability to capture the behavior of the plume related to aircraft sources during LTO cycles at an airport, while comparing with observations that are available, and identifying strengths and weaknesses compared to another existing model.
- In collaborating with Boston University (BU), we will rely on BU to perform appropriate clean-up and quality assurance/quality control (QA/QC) of observation data before using it in our model evaluation routines. We will also work closely with BU to ensure appropriate and careful interpretation of the data. UNC and BU have collaborated extensively on similar projects in the past, and we expect to have robust model measurement and modeling assessment from the BOS study.

5) **Prepare AEDT Emissions Inventories**
   - To support this task, we will obtain aircraft operations data from the FAA and use the latest public version of AEDT to create BOS-specific airport-level emissions inventory corresponding to the measurement campaign period.

Task 2 – Develop and Evaluate a Multiscale WRF-SMOKE-CMAQ Model Application for BOS Focused on UFP

University of North Carolina at Chapel Hill

Objectives

In this task, we will collaborate with ASCENT 18 investigators at BU with a specific focus on modeling BOS at multiple spatial scales and perform intercomparison of the measurement and modeling with a focus on ultrafine particulate matter, mass and number concentrations, due to aircraft emissions. Using airport-specific inventories (see additional discussion below), we previously started to explore the use of two modeling approaches: CMAQ and the SCICHEM model. The SCICHEM model incorporates complete gas, aqueous, and aerosol phase chemistry within a state-of-the-science Gaussian puff model SCIPUFF (Second-order Closure Integrated Puff; Chowdhury et al., 2015). Since SCICHEM uses the same aerosol treatment as CMAQ but is able to characterize aircraft impacts at very fine scales around the airport, a key project outcome is the ability to improve aircraft-attributable PM on prior estimates. Note that because SCICHEM only predicts PM mass concentrations, we will develop post-processing routines to convert PM mass to particle number concentration (PNC) using the same approach as in CMAQ before model validation. Also, SCICHEM has not been used to predict PNC to date; therefore, this will be a new direction in research.

During spring and summer of 2017, ASCENT 18 investigators made multiple measurements of ultrafine particles (UFP) and black carbon at various locations south and west of BOS. Since then, an entire year of data on both UFP and black carbon have been collected for 2018. We will collaborate with BU to obtain these measurements to perform intercomparison against model outputs.

To support this modeling study, we will explore the use of obtaining BOS-specific airport-level emissions inventories from AEDT for 2018 from Massport, the public authority that manages BOS. If not available during the proposed period of performance, we will use existing AEDT-based full-flight aircraft inventories from one of the global-scale 2018 inventories that FAA/Volpe may have and extract BOS operations during LTO phases to support this assessment.

In this task, we will create a 12/4/1-km nested application of the Weather Research Forecast (WRF)–Sparse Matrix Operator Kernel Emissions (SMOKE)–CMAQ modeling system for two seasons (summer and winter) and simulate two emissions scenarios:

- Background emissions from all sources except BOS
- Background + BOS airport emissions during LTO cycles

Next, we will perform multiple sensitivity simulations with CMAQ v5.3 base and v5.3 augmented with the new nucleation mode described by Murphy et al. (2017). Specifically, this study adds a third mode in addition to the Aitken and Accumulation modes that have been historically used in all CMAQ applications to date.

The emissions inventories for nonaviation sectors for this application will rely on the EPA's National Emissions Inventories (NEI) for the year 2018 (if available) or projected from the NEI-2017. The meteorological fields will be downscaled from NASA's Modern-Era Retrospective Analysis for Research and Applications (MERRA) v2 (Reinecker et al., 2011).

The base CMAQ model application will be configured as follows:

a) Aircraft emissions from AEDT processed through AEDTProc;
b) Background emissions from NEI processed through SMOKE v3.6;
c) Meteorology from MERRA downscaled with WRF v3.8;
d) Lightning NOx;
e) Inline photolysis; and
f) Latest version of CMAQ (v5.32) but enhanced with the new aircraft-specific emissions module as described in Huang et al. (2017).

The initial and boundary conditions for the outermost grid (12 km) will be downscaled from CMAQ applied at the Northern Hemisphere at the 108-km resolution. The subsequent 4 km and 1 km grids will be nested down appropriately from the immediate outer grid as is standard practice.

After the model application has been developed and evaluated, UNC will obtain 2017–2018 field observations from the ASCENT 18 team at BU and perform model measurement comparisons. Previously in 2017, BU captured measurements at five fixed-site locations on the arrival path of aircraft at BOS. We will collaborate with BU on this task and compare regression and dispersion model-based assessments of UFP from BOS. As can be seen above, this is a collaborative effort with the ASCENT 18 investigators that will require constant exchange of information and sharing results throughout the period of performance, which will lead to an integrated measurement and modeling-based assessment of UFP due to aircraft emissions at BOS.

Research Approach

In this research, we describe progress made on the two tasks.

Task 1: Develop and Evaluate a New Dispersion Model for Aircraft Sources

1. Source Characterization

1.1 Aircraft Source Characterization in AERMOD

Modeling aircraft dispersion near the surface is challenging because aircraft are dynamic mobile sources that emit pollutants at varying rates depending on the operating mode. In 2005, the U.S. EPA adopted AERMOD, the most recent version of short-range steady-state atmospheric dispersion model for air quality regulatory purposes. AERMOD (v04300) was promulgated into EDMS (Emissions and Dispersion Modeling System; Martin, 2006) by the U.S. EPA in 2006, and EDMS was replaced by the FAA's AEDT (FAA, 2014) in May 2015, despite the fact that AERMOD was not designed to model elevated mobile sources. The representation of mobile sources, such as motor vehicles and the aircraft LTO cycle, has traditionally consisted of a series of AREA or VOLUME sources placed at various heights, and recently AERMOD (v21112) included an option to model on-road mobile sources as LINE segments. The publicly released version of FAA's AEDTv3e models aircraft emissions as a series of AREA source segments. This new version also has a key feature that allows users to model aircraft sources, both fixed wing and rotorcraft, as a series of VOLUME sources. Here we describe an evaluation of AERMOD predictions when modeling aircraft sources as AREA vs. VOLUME sources, along with a detailed comparison of spatial-temporal patterns in emissions.

The case study for this evaluation is LAX. We used datasets from the summer campaign (July 18 to August 28, 2012) from the LAX AQSAS (Arunachalam et al., 2017a; Tetra Tech, 2013).

We summarize below the various comparisons that we performed to quantify emissions estimates when using the AREA-and VOLUME-based treatments, and then the AERMOD-based concentration predictions of SO_2 for these two treatments.

1.1.1 Emissions and Source Parameter Comparisons

Based on the height and LTO cycle, we divided all AERMOD sources into the following five categories: AIRG620M (at height 619.2 m), AIRL620M (at height less than 619.2 m), GATE (at height 1.5 m), RUNWAY (at height 12 m lying on runways), and

TAXI (at height 12 m).

We compared the number of sources on AREA and VOLUME treatment files and found that the VOLUME source treatment file has a large number of sources at each category defined above except the GATE sources. The source characterization of GATE sources is similar in both files as AREA-POLYGON. In the VOLUME source file, the number of TAXI sources was13 times greater compared with the AREA source file (Table 1). The reason for the higher number of VOLUME TAXI sources is because for AREA sources, each TAXI link is assigned as a single AREA source (as a rectangle), but for VOLUME sources, each TAXI link is divided into 20 × 20 squares (Figure 1). However, the number of RUNWAY and airborne sources increased, respectively, by 38% and 41% in the VOLUME treatment file compared with the AREA treatment file (Table 1).

Irrespective of the greater number of sources in the VOLUME source treatment file, the SO_2 emissions (ton/period) were identical in both files for all five categories (Table 1). The average hourly total emissions in both the files were also identical at each hour for each category (Figure 2). The total average hourly emission for all five categories is high at around 16 g/s at hour 14 and lowest at hour 4 in both files (Figure 3).

Source parameters are given in Table 2 for both source treatments. The initial vertical dispersion parameter (σ_{z_0}) for all VOLUME sources is increased from 4.1 m (AREA source treatment) to 14 m. GATE source characterization is similar to AREA-POLYGON in both source files, and σ_{z_0} is 3 m for these sources (Table 2). The main reason behind the change in initial vertical dispersion parameter here is that the VOLUME sources are broken out by airframe-engine type and mode to allow for different initial dispersion parameters for each combination.

Table 1. Quantitative comparison of AREA and VOLUME source treatment files.

Source Group	Release Height (m)	Number of Sources in Each File		SOx Emissions (ton/period)	
		AREA	VOLUME	AREA	VOLUME
AIRG620M	Hs = 619.2 m	19,013	26,296	11.91	11.91
AIRL620M	Hs <619.2 m	4,729	7,142	5.81	5.81
RUNWAY	12 m	2,593	3,569	6.00	6.00
TAXI	12 m	248	3,320	14.01	14.01
GATE	1.5 m	21	21	1.19	1.19
Total	All	26,604	40,348	38.92	38.92

Table 2. Source parameters at each category in AREA and VOLUME source treatment files.

Source Group	Release Height (m)	AREA				VOLUME	
		Length (m)	Width (m)	Angle (°)	$\sigma_{z_0}(m)$	$\sigma_{y_0}(m)$	$\sigma_{z_0}(m)$
AIRG620M	Hs = 619.2 m	200	200	0	4.1	46.51	14
AIRL620M	Hs < 619.2 m	200	200	0	4.1	46.51	14
RUNWAY	12 m	20	20	0	4.1	4.65	14
TAXI	12 m	22.86	variable	variable	4.1	4.65	14
GATE	1.5 m	AREA-POLYGON			3	AREA-POLYGON	3

(a) AREA Treatment (TAXI)

(b) VOLUME Treatment (TAXI)

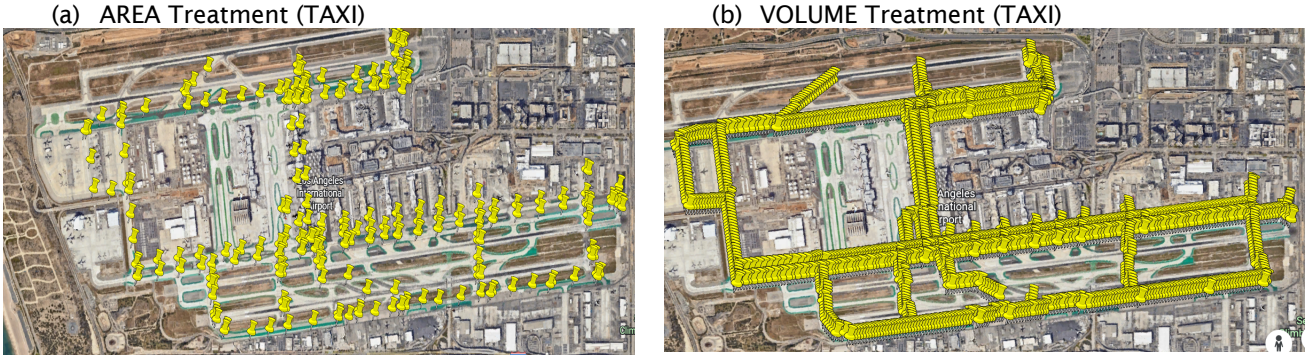

Figure 1. TAXI source locations in (a) AREA and (b) VOLUME source treatment files.

(a) AREA Source Treatment

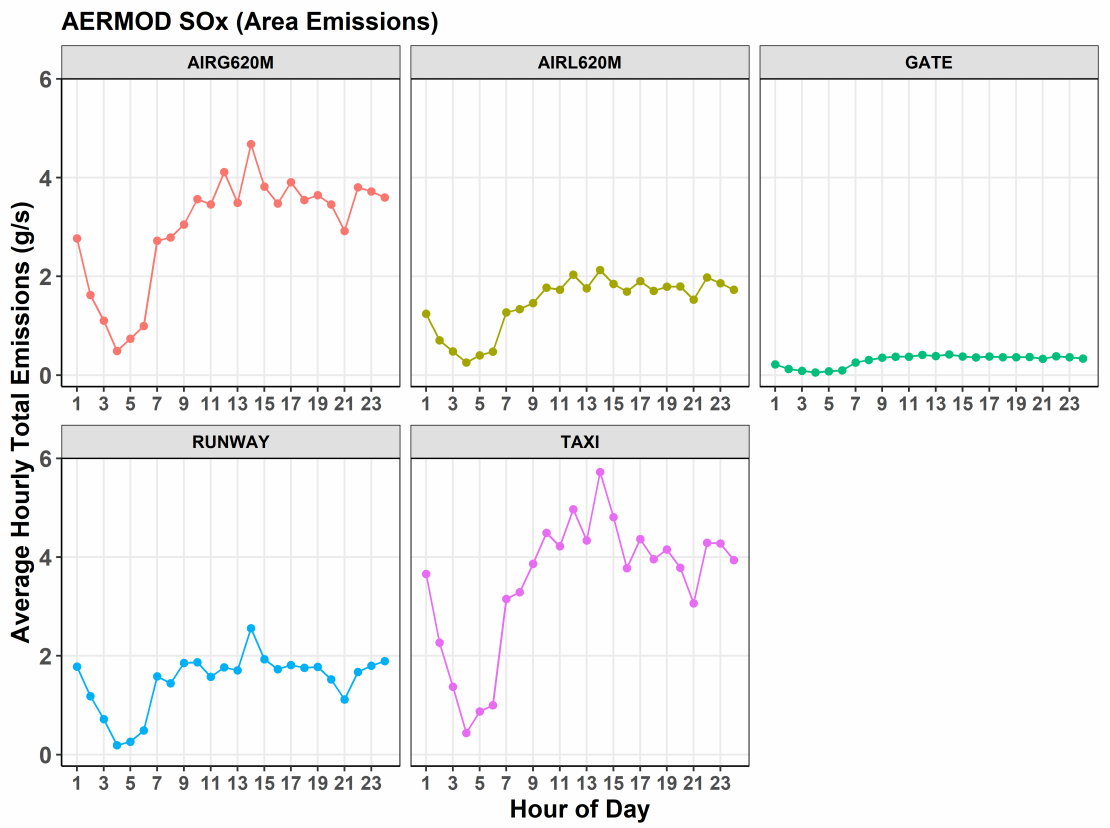

(b) VOLUME Source Treatment

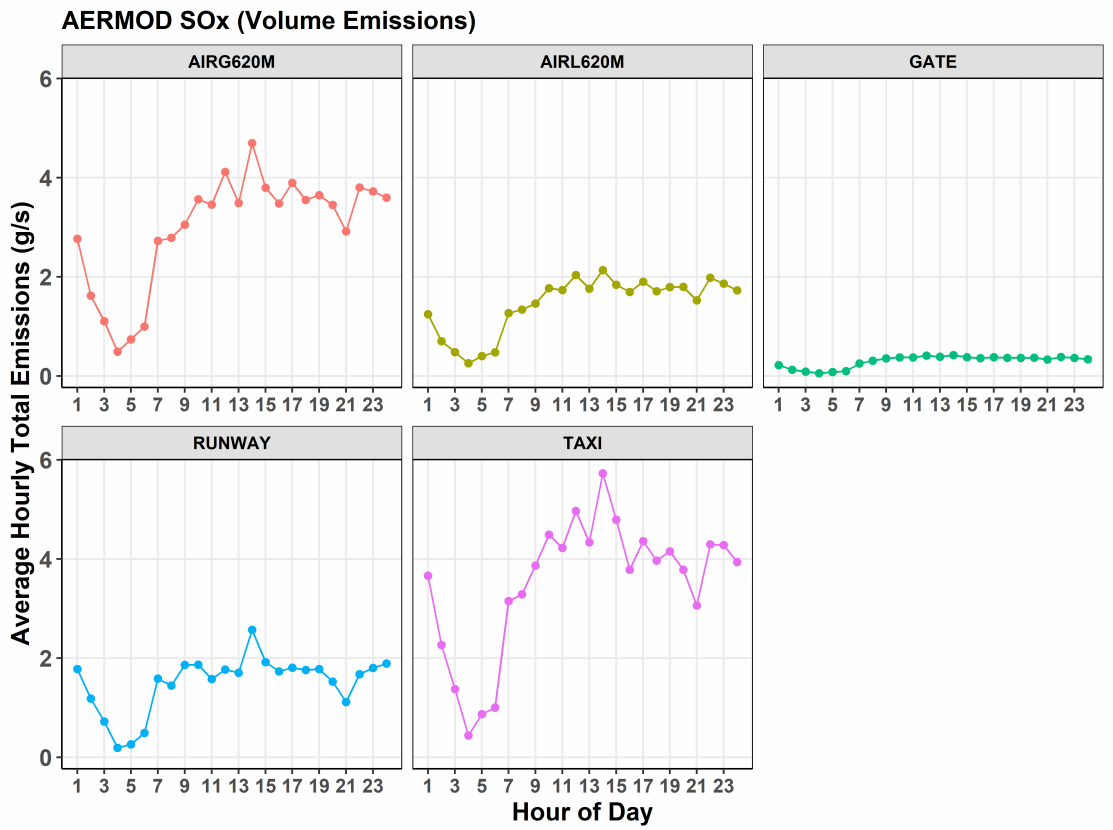

Figure 2. Average hourly total emissions at each hour in (a) AREA and (b) VOLUME treatment files for all five categories (AIRG620M, AIRL620M, GATE, RUNWAY, and TAXI).

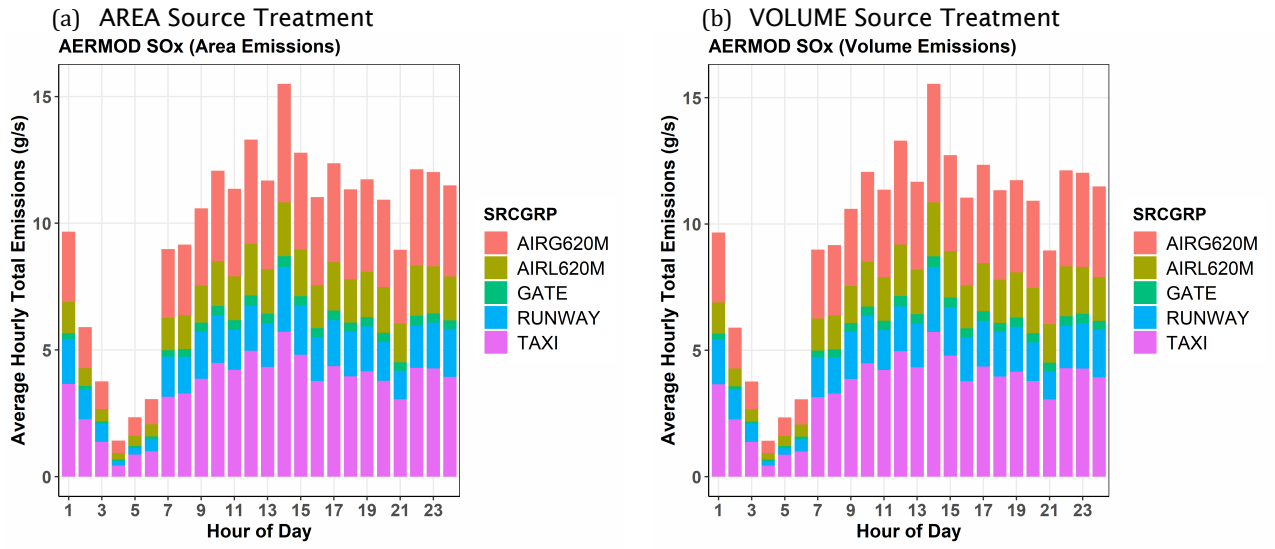

Figure 3. Average hourly total emissions at each hour in (a) AREA and (b) VOLUME treatment files for all five categories (AIRG620M, AIRL620M, GATE, RUNWAY, and TAXI).

1.1.2 Concentration Comparisons Using AERMOD (V21112):

To compare model performance using both source treatment files, we utilized the AERMOD (v21112) dispersion model and ran the model for aircraft sources only using the existing summer meteorological files for LAX. For the modeled concentration comparison using both files, we used the diurnal and quantile-quantile (Q-Q) distribution plots with a few EPA-recommended statistical parameters such as FAC2 (factor of 2 to the observation), FB (fractional bias [standard in diurnal plot and based on top 26 robust highest concentrations in QQ plot; Cox and Tikvart, 1990]), R (correlation coefficient), and PR (peak ratio; the ratio of highest modeled concentration to highest observed concentration) at four core sites, namely Air Quality (AQ), Community North (CN), Community South (CS), and Community East (CE) of LAX.

At all four core sites in the diurnal plots, neither source file was able to predict the concentration close to observation. There was high over-prediction in the morning at AQ and CS, and high over-prediction in the late evening at CN, CS, and CE sites (Figure 4a). However, both source treatment files had similar characteristic features at all four core sites (Figure 4a). There was a slight improvement in all statistical measures using the VOLUME source treatment (Figure 4a).

In Q-Q plots at all four sites, the higher concentrations declined slightly, and lower concentrations increased and came close to FAC2 lines using the VOLUME source treatment compared to the AREA source treatment (Figure 4b). In quantitative terms, the FB was improved using VOLUME source treatment (Figure 4b).

1.1.3 Sensitivity Analysis Based on Initial Vertical Dispersion Parameter

In addition, we performed a sensitivity analysis based on the initial vertical dispersion parameters (σ_{z_0}) in both source treatment files:

a) Changed the σ_{z_0} values from 4.1 m to 14 m for all surface, airborne, and taxi sources in AREA source file.
b) Changed the σ_{z_0} values from 14 m to 4.1 m for all the surface, airborne, and taxi sources in VOLUME source file.

In this sensitivity analysis, when we increased σ_{z_0} from 4.1 m to 14 m in the AEDT-generated AERMOD AREA source treatment file, we found that the modeled higher concentrations declined slightly; we can easily see this from the change in FB values (Figure 5b). In contrast, when we decreased σ_{z_0} from 14 m to 4.1 m in the AEDT-generated VOLUME source treatment file, there was a slight increase in FB that suggested an increase in the modeled concentration (Figure 6b). However, in both sensitivity analyses, the diurnal characteristic features did not change after an increase or decrease in σ_{z_0} values, except for a slight change at high concentrations, which can be seen by the change in FB values (Figures 5a and 6a).

Overall, we found better performance by VOLUME source treatment. However, from this improved performance arose the following two questions, which are addressed in the next section:

a) Is improved performance due to the increase in the number of sources in VOLUME source treatment?
b) Is improved performance due to the source characterization (meander component in VOLUME source)?

1.1.4 Conversion of AREA to VOLUME and VOLUME to AREA (UNC)

To check the above-mentioned concerns, we converted the AEDT-generated AREA and VOLUME source files into VOLUME and AREA source files. This was done by converting the emissions and taking the appropriate source parameters as per Table 2 for each source. At UNC using an R script, we converted AEDT-generated AREA and VOLUME source input files into VOLUME and AREA source files. The main key findings from this conversion analysis are as follows:

a) AREA to VOLUME/VOLUME to AREA conversion showed that AERMOD predictions are better when using VOLUME source treatment (Figures 7 and 8).

b) As the number of sources is the same after each conversion, all improvements in model predictions were shown to be due to the VOLUME source treatment (Figures 7 and 8).

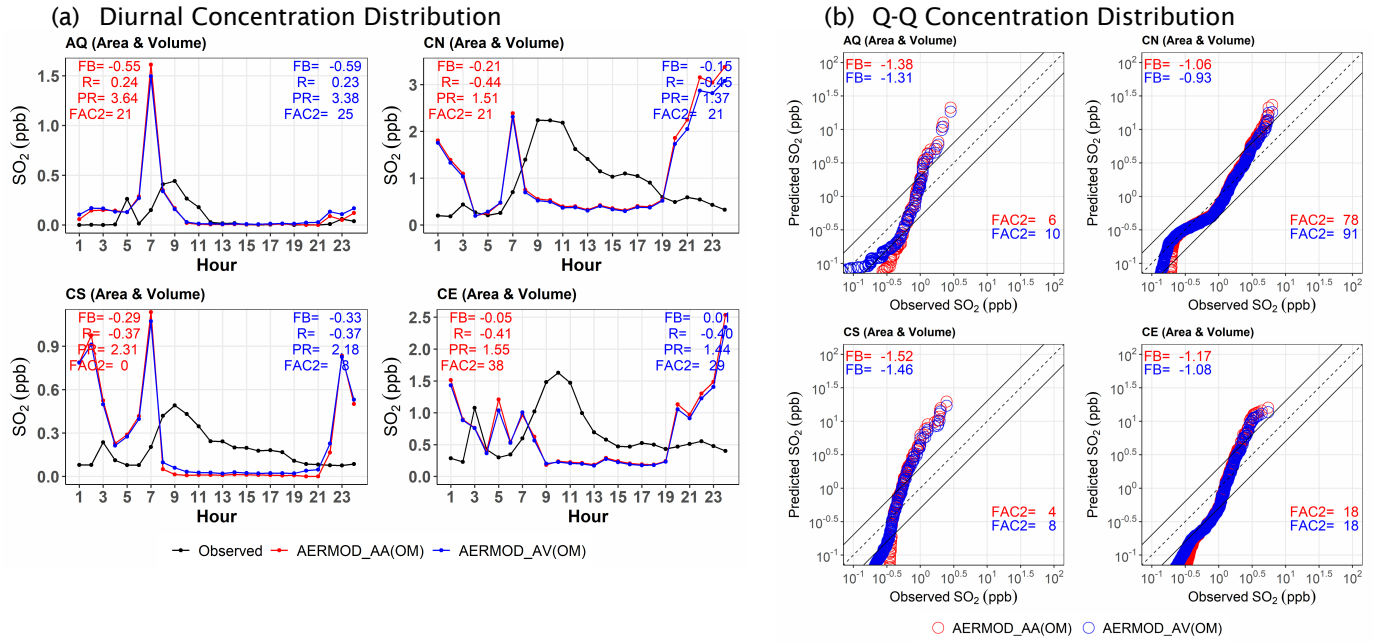

Figure 4. (a) Diurnal variability in observed and modeled SO_2 concentrations, (b) quantile-quantile (Q-Q) concentration distribution between observed and modeled SO_2 concentrations files at all four core sites (AQ, CN, CS, and CE) using AEDT-generated AREA and VOLUME source treatment. OM, original meteorology; AA, AEDT-generated AREA source file; and AV, AEDT-generated VOLUME source file.

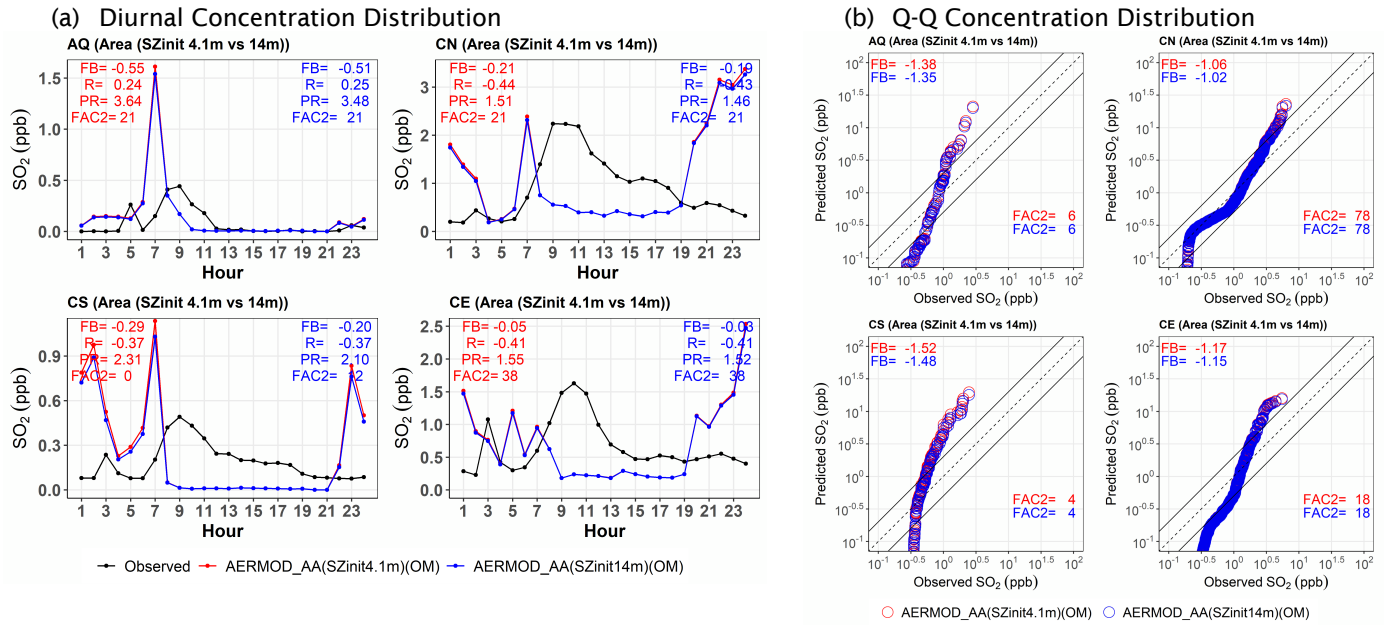

Figure 5. (a) Diurnal variability in observed and modeled SO_2 concentrations, (b) quantile-quantile (Q-Q) concentration distribution between observed and modeled SO_2 concentrations files at all four core sites (AQ, CN, CS, and CE) using AEDT-generated AREA source treatment. OM, original meteorology; AA, AEDT-generated AREA source file; SZinit, initial vertical dispersion parameter (σ_{z_0}).

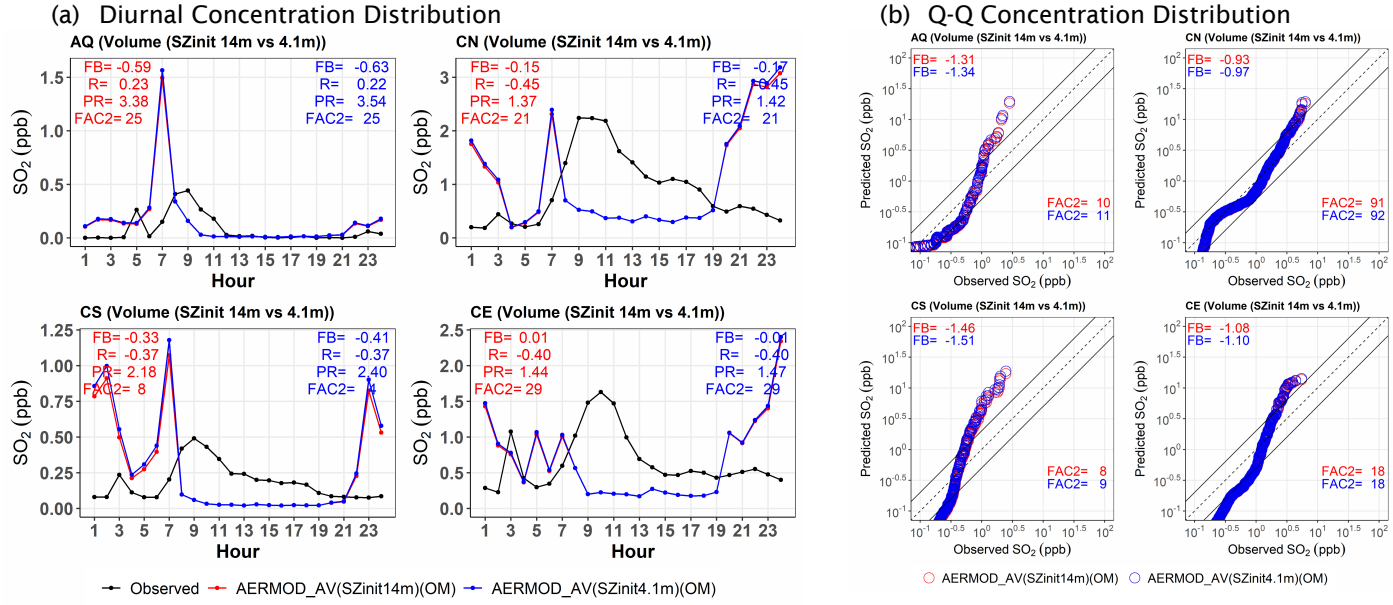

Figure 6. (a) Diurnal variability in observed and modeled SO_2 concentrations, (b) quantile-quantile (Q-Q) concentration distribution between observed and modeled SO_2 concentrations files at all four core sites (AQ, CN, CS, and CE) using AEDT-generated VOLUME source treatment. OM, original meteorology; AV, AEDT-generated VOLUME source file; SZinit, initial vertical dispersion parameter (σ_{z_0}).

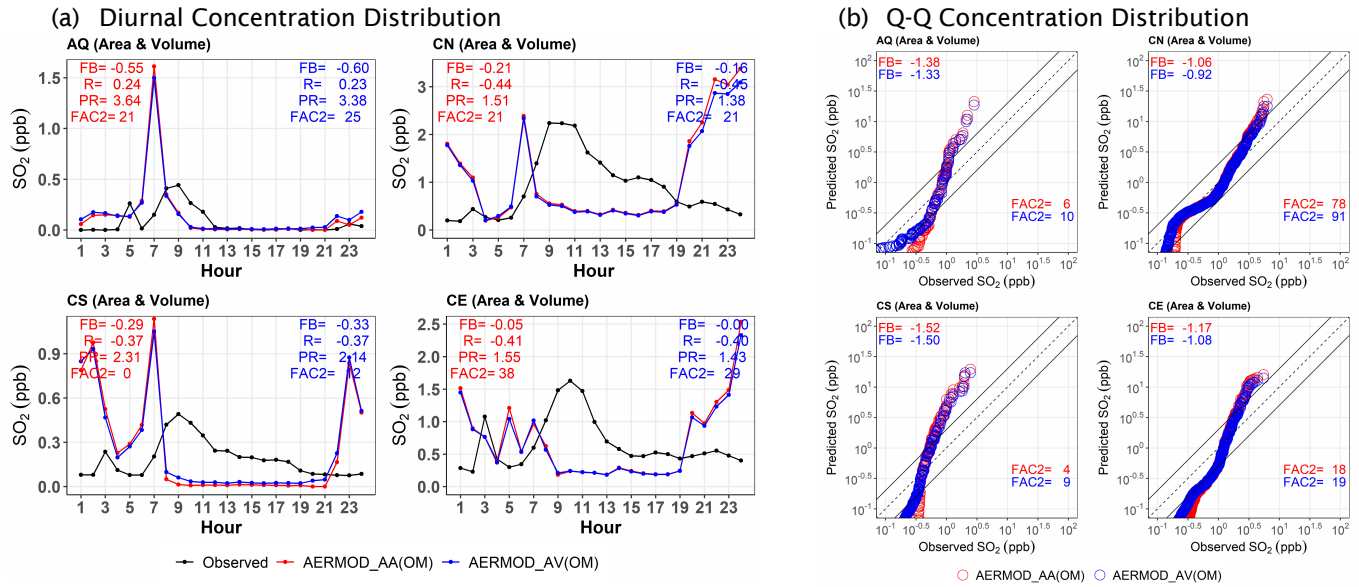

Figure 7. (a) Diurnal variability in observed and modeled SO_2 concentrations, (b) quantile-quantile (Q-Q) concentration distribution between observed and modeled SO_2 concentrations files at all four core sites (AQ, CN, CS, and CE) using AEDT-generated AREA source treatment and UNC-converted VOLUME source treatment file from AEDT-generated AREA source file. OM, original meteorology; AA, AEDT-generated AREA source file; AV, UNC-converted VOLUME source file.

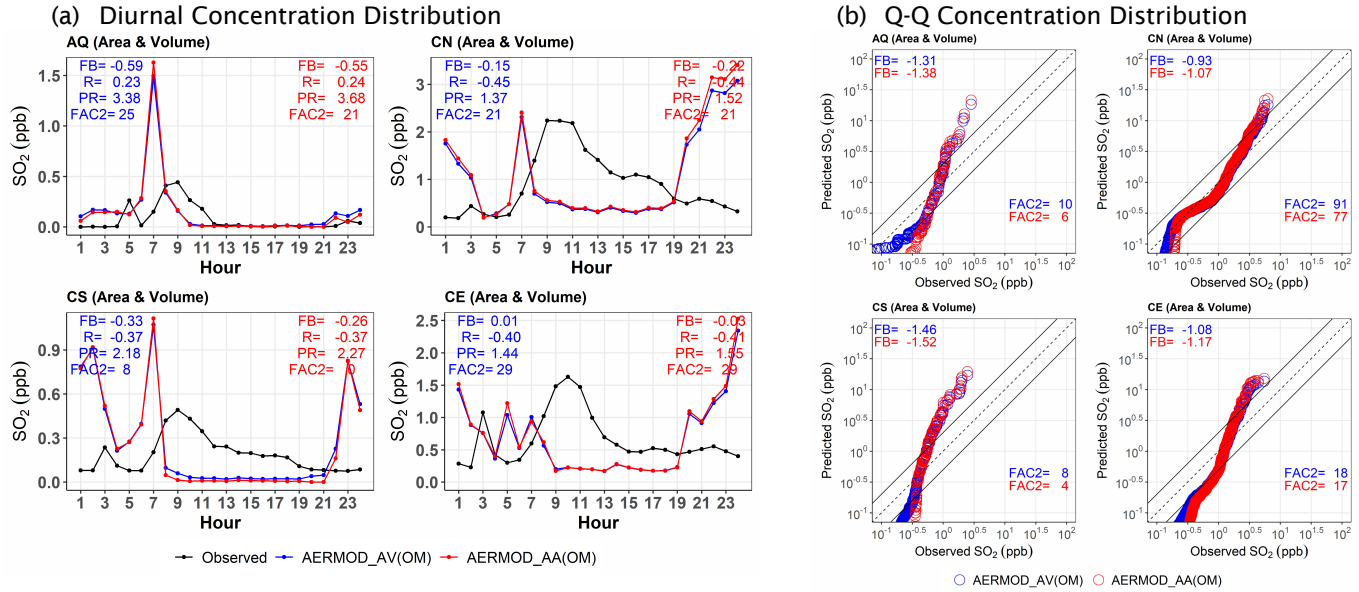

Figure 8. (a) Diurnal variability in observed and modeled SO_2 concentrations, (b) quantile-quantile (Q-Q) concentration distribution between observed and modeled SO_2 concentrations files at all four core sites (AQ, CN, CS, and CE) using AEDT-generated VOLUME source treatment and UNC-converted AREA source treatment file from AEDT-generated VOLUME source file. OM, original meteorology; AV, AEDT-generated VOLUME source file; AA, UNC-converted AREA source file.

1.1.5 Summary

Here, we found that VOLUME source treatment had a greater number of sources than AREA source treatment. Irrespective of the greater number of VOLUME sources, emissions were identical at each mode in both treatment files. The key finding is that AERMOD model predictions improved slightly for higher concentrations and significantly for lower concentrations through VOLUME source treatment. In quantitative terms, VOLUME source treatment has less FB (based on robust highest concentrations (RHC)). Hence, VOLUME source treatment is slightly better than AREA. To check this, we performed sensitivity analyses based on the increase/decrease in initial vertical dispersion parameter and conversion from AREA/VOLUME to VOLUME/AREA. At each conversion, the number of sources did not change, and the overall results suggest that all improvements at the lower end of model predictions were due to the meander component of VOLUME source, and that improvements at higher concentrations were due to the increase in the initial vertical dispersion parameter (σ_{z_0}) from 4.1 m to 14 m. However, all sensitivities suggest that VOLUME source treatment was better than AREA source treatment.

1.2 AEDT2ADM Tool

A Python-based emission processor called "AEDT2ADM" has been developed that can produce emission files of the new ADM and AERMOD dispersion models using the AEDT's flight segment data. We have updated the emission processor and evaluated the flight segment data of both AEDT winter and summer 2012 files.

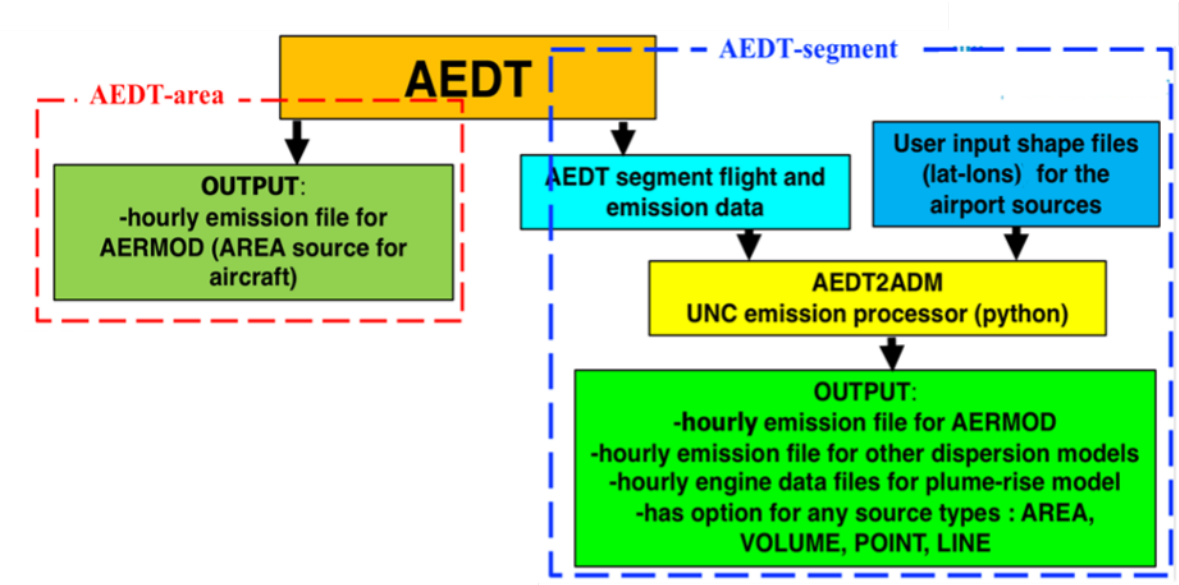

Figure 9: The schematic of input/output data flow off AEDT2ADM emission processor.

1.2.1 Update of the AEDT2ADM Emission Processor

The AEDT2ADM emission processor has been updated to include multiple new features since the last version reported in UNC's ASCENT 2021 annual report. The new updates are described below as follows:

a) We cleaned the 2021 version AEDT2ADM code and put this whole package into a private GitHub repository and shared it with FAA. Now, the AEDT2ADM emission processor has been updated and it can produce emission input files of ADM as well as AERMOD models for all species present in the AEDT-segment files for each day for the entire time period in a single run. From Figure 9, we can see how this processor works to generate AERMOD- and ADM-ready input files.

b) In the 2021 version, we updated the spatial resolution capability of the surface sources based on users' specific latitude and longitude of runways and gateways. In the current 2022 version, we updated the spatial resolution of airborne sources. Previously, there were only 144 fixed airborne point sources based on nine fixed layers; this new airborne source methodology starts with the extent of the ground sources and user-provided latitude/longitude

sources of the full domain to create an inverted pyramid grid with increasing grid-cell sizes. This allows ADM to use the same number of sources for all days of a modeling run (Figure 10 and Table 3).

c) We added new functionality to generate gridded surface source files as well as emission and engine parameter files for an additional feature within ADM. With this additional feature, ADM can use a simple short-range gridded dispersion model, which could be better in low and variable wind dispersion cases.

d) AEDT2ADM is also updated to generate the engine parameters files for ADM. Winter AEDT-segment data do not include taxi speed so we have used the average summer season taxi speed to calculate aircraft speed. Negative thrust values in the AEDT-segment data are replaced by 7% of maximum thrust while aggregating hourly data for ADM inputs.

e) Apart from the above AEDT2ADM updates, we reported several issues in the FAA/Volpe-provided segment and AERMOD-ready input files for LAX. All issues are summarized in each month's report.

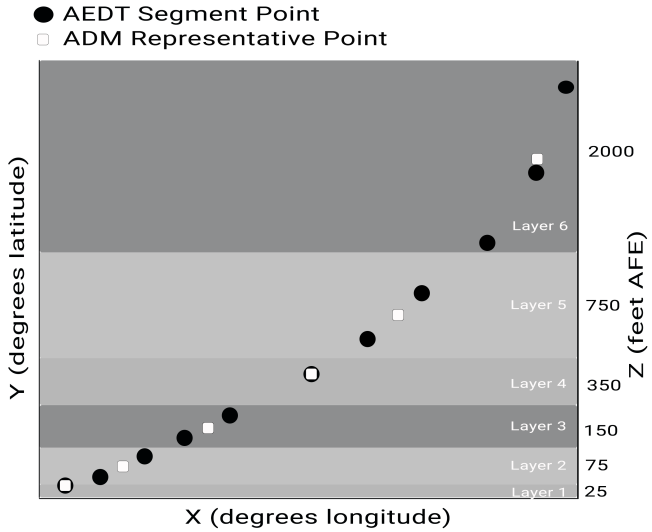

Figure 10. Schematic of new airborne source methodology.

Table 3. Layer-wise airborne source distribution based on grid sizes.

Layer	Grid Size (m)	Top of Layer (ft)	Number of sources
1	250	50	612
2	350	100	1,152
3	575	200	903
4	975	500	578
5	1,600	1,000	338
6	2,000	3,000	512
		Sources	4,095
		Sources with directions	8,190

2. Physical Processes

2.1 Aircraft's Plume Rise Algorithm Development and Implementation in AERMOD

In view of the incompleteness of the dispersion models used in aircraft dispersion modeling, we have developed a plume rise algorithm for turbojet and shaft-based aircraft engines. In the 2021 UNC ASCENT report, we mentioned only the simple algorithm to calculate plume rise for turbojet engines. We have now substantially updated this algorithm and developed a new algorithm for shaft-based engines for surface and airborne aircraft sources. It builds upon our current understanding of plume rise of emissions from stationary point sources and can be readily incorporated into AERMOD or the new ADM.

The buoyancy parameter, F_b, that governs plume rise from a point source is associated with energy output from an aircraft engine. The buoyancy parameter, F_b, of the exhaust plume is given by the following expression (Briggs, 1965):

$$F_b = \frac{g}{T_a} v_e r_0^2 (T_e - T_a), \quad (1)$$

where v_e and T_e are the velocity and temperature, respectively, of the exhaust plume, T_a is the ambient temperature, and g is the acceleration due to gravity. The plume rise, h_{pb}, associated with a buoyant release from a point source in a neutral atmosphere is given by (Briggs, 1965)

$$h_{pb} = \left(\left(\frac{r_0}{\beta}\right)^3 + \frac{3}{2\beta^2} \frac{F_b}{U_{eff}^3} x^2 \right)^{1/3} - \left(\frac{r_0}{\beta}\right), \quad (2)$$

where $\beta = 0.6$ is an entrainment constant, x is the effective distance between the source and receptor, U_{eff} is the effective velocity within the plume, and r_0 is the initial radius of the plume.

Generally, there are two types of engines in aircraft: jet/gas turbine and piston engines (Figure 11). Here, we have divided all engine types into two categories to calculate the plume rise. The first category is based on the known bypass ratio (turbojet and turbofan engines), and the second one does not have a known bypass ratio (turboprop, turboshaft, and piston engines).

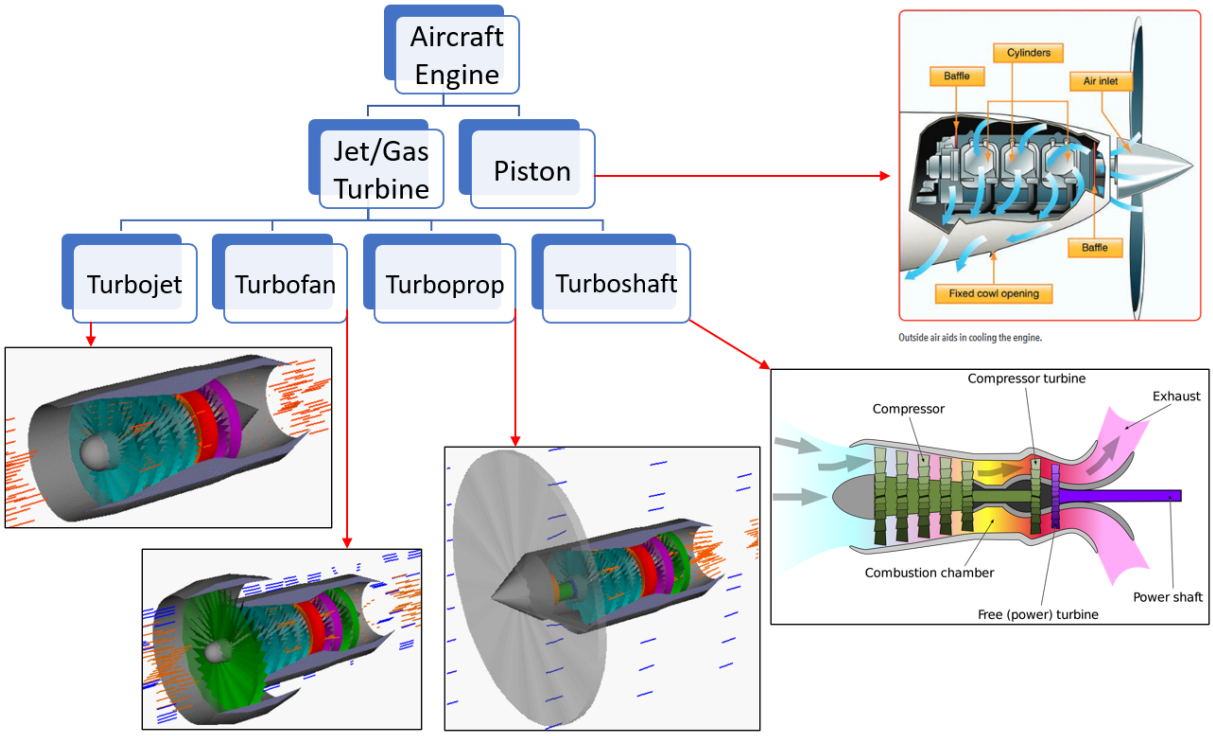

Figure 11. Aircraft engine types and working (Source: NASA).

2.1.1 Category 1

This category consists of two jet/gas turbine engines such as turbojet and turbofan engines. When the aircraft is moving, air enters the engine at the speed of the aircraft relative to the aircraft. A fraction of the incoming air is directed into the core, where it is first compressed, then enters the combustion where the injected fuel increases the temperature of the gases, which then drives a gas turbine. The gas turbine generates enough power to drive the compressor and the fan. The core flow is then exhausted through a nozzle. Figure 11 shows the operation of a modern turbofan/turbojet engine. Most of the air entering the engine "bypasses" the core as it is driven toward the exit by the fan at the entrance. The mass flow rate of the bypass air is several times that of the core air; the ratio of the two mass flow rates is known as the bypass ratio, which we denote here by $bypr$. The bypass ratio of modern turbofan engines is >5. The exiting air is a mixture of core air and bypass air, and the average velocity of the two streams is much smaller than that of the core air. Low-bypass turbofans are commonly used in fighter jet engines and have ratios in the 0.30 to 0.50 range, whereas modern high-bypass engines may have a ratio as high as 9 or 10.

The thrust of the engine is the product of the total mass flow rate and the difference between the inlet and exit velocities. As we will see, the power associated with propulsion is maximized by bringing the exit velocity of the exhaust gases as close as possible to the inlet velocity and, at the same time, increasing the mass flow rate through the engine. This is achieved through as large a bypass ratio as possible, which requires making the fan as large as possible.

The ratio of the mass of air entering the core to that of the fuel injected into the combustion chamber is known as the air-fuel ratio, denoted here by AF. Although the stoichiometric AF ratio is about 15, it is maintained at values >45 to ensure that the temperature of the gases exiting the combustion chamber is below that required for the integrity of the turbine blades. The ratio of the mass flow rate of air plus fuel, $\dot{m}$, to that of the fuel, $\dot{m}_f$, is approximately $AF(1+bypr)$, which is >200 for most aircraft engines. Therefore, the mass flow rate through the engine is essentially that of air. We now have the background to relate the buoyancy parameter to the characteristics of an aircraft engine.

2.1.1.1 Computing the Buoyancy Parameter From Engine Characteristics

The exhaust gas velocity and temperature required in Equation (1) to compute the buoyancy parameter are not available for jet/gas turbine engines. Thus, it is necessary to estimate the buoyancy parameter using variables used to characterize jet engines. These variables are the engine thrust, *T*, the aircraft velocity, v_a, fuel burn rate, $\dot{m}_f$, the air-fuel ratio, *AF*, and the bypass ratio, *bypr*. We show below how these variables are used to estimate the buoyancy parameter, which can be written in terms of Q_e, the thermal power added to the air passing through the engine:

$$F_b = \frac{g}{T_a}\frac{Q_e}{\pi\rho_e C_p}, \tag{3}$$

where ρ_e is the exhaust density, and C_p is the specific heat of the exhaust gases, which is mostly air.

We can derive an expression for Q_e by writing the energy balance:

$$\dot{m}_f H_f = \frac{\dot{m}}{2}(v_e^2 - v_a^2) + Q_e, \tag{4}$$

where $\dot{m}_f$ is the fuel consumption rate, and H_f is the heating value of the fuel. Equation (4) states that the power supplied by the fuel (left-hand side) is the sum of the increase in kinetic power and thermal power added to the air passing through the engine. Rearranging the equation gives

$$Q_e = \dot{m}_f H_f \left(1 - \frac{\dot{m}}{2}\frac{(v_e^2 - v_a^2)}{\dot{m}_f H_f}\right). \tag{5}$$

The second term within the parentheses on the right-hand side is the thermal efficiency, defined by

$$\eta_t = \frac{\dot{m}}{2}\frac{(v_e^2 - v_a^2)}{\dot{m}_f H_f}, \tag{6}$$

which can be expressed in terms of the thrust, T, and the exhaust velocity, v_e, of the gases from the engine

$$T = \dot{m}(v_e - v_a), \tag{7}$$

where v_e is the exhaust velocity, v_a is the aircraft velocity, and $\dot{m}$ is the mass flow rate of air plus fuel. Substituting Equation (7) in (6) yields

$$\eta_t = \frac{T(v_e + v_a)/2}{\dot{m}_f H_f} = \frac{T v_{avg}}{\dot{m}_f H_f}, \tag{8}$$

where the average velocity, $v_{avg} = (v_e + v_a)/2$. Thermal efficiency can be written in terms of overall efficiency, η_o, and the propulsive efficiency, η_p.

The overall efficiency η_o, is the ratio of the propulsive power, Tv_a, to the power derived from the fuel:

$$\eta_o = \frac{Tv_a}{\dot{m}_f H_f}. \tag{9}$$

The propulsive efficiency, η_p, is the ratio of the propulsive power to the power associated with kinetic energy imparted by the engine:

$$\eta_p = \frac{Tv_a}{\dot{m}(v_e^2 - v_a^2)/2} = \frac{\dot{m}(v_e - v_a)v_a}{\dot{m}(v_e - v_a)v_{avg}} = \frac{v_a}{v_{avg}}. \tag{10}$$

Substituting Equations (9) and (10) into Equation (8) results in

$$\eta_t = \frac{\eta_o}{\eta_p} \text{ and}$$
$$\eta_o = \eta_t \eta_p. \tag{11}$$

We see that calculation of thermal efficiency, η_t, requires an estimate of the exhaust velocity, v_e, which can be obtained from Equation (7):

$$v_e = v_a + \frac{T}{\dot{m}}, \tag{12}$$

and the total mass flow rate, $\dot{m}$, is related to the fuel burn rate, $\dot{m}_f$, through

$$\dot{m} = \dot{m}_f AF(1 + bypr), \tag{13}$$

where AF is the air-fuel ratio, and $bypr$ is the engine bypass ratio.

Then, the preceding equations allows us to compute the buoyancy parameter, F_b, from

$$F_b = \frac{g}{T_a} \frac{\dot{m}_f H_f (1 - \eta_t)}{\pi \rho_e C_p}, \tag{14}$$

where the exit density, ρ_e, is computed from the energy conservation equation and the equation of state,

$$T_e = T_a + \frac{Q_e}{\dot{m} C_p}$$
$$\rho_e = \frac{p_a}{R_a T_e}, \tag{15}$$

where T_e is the average temperature of the exhaust gases, p_a is the ambient pressure, and R_a is the gas constant of air. We see that the inputs required to compute F_b are the thrust, T, the aircraft velocity, v_a, the fuel burn rate, $\dot{m}_f$, the air-fuel ratio, AF, and the engine bypass ratio, $bypr$.

2.1.2 Category 2

This category has two jet/gas turbine engines such as turboprops and turboshaft, and it consists of a third type: piston engines. These engines do not have known bypass ratios.

Turboprops extract virtually all the kinetic energy and a larger portion of the thermal energy via expansion turbines to drive the propeller, whereas turbofans utilize an expansion nozzle to create high-speed exhaust (thrust) (Figure 11). For turboprops, very little thrust is produced by the exhaust directly (2%-3% of total thrust output); the propeller does the work of converting heat to thrust via a gearbox driven by the expansion turbine. It can be useful to think of turboprops as unducted turbofans in some sense, where the propeller is the first fan in the compressor section. However, it should be noted that there is no actual bypass air for a turboprop engine. This analogy breaks down in a mechanical sense but is useful in the aerodynamic and thermodynamic sense. The ideal turboprop would convert all the exhaust's energy into mechanical work to drive the propeller.

The turboshaft engine is another common type of jet/gas turbine engine. It delivers power to a shaft that drives something other than a propeller. The biggest difference between a turbojet and turboshaft engine is that on a turboshaft engine, most

of the energy produced by the expanding gases is used to drive a turbine rather than produce thrust. Many helicopters use a turboshaft gas turbine engine. In addition, turboshaft engines are widely used as auxiliary power units on large aircraft. Turboshaft engines and piston engines do not have a known bypass ratio. We could calculate a bypass ratio for a given engine/propeller configuration, but because manufacturers can install propellers of arbitrary diameter and blade count on a particular engine, we cannot know this value as a function of the engine itself. We could potentially determine a bypass ratio for a particular application (i.e., a propeller or rotor of a known diameter) of a turboshaft engine used on a helicopter by assigning the "bypass" air transported through that known propeller or rotor.

2.1.2.1 Computing the Buoyancy Parameter From Engine Characteristics

In a turboshaft engine, the propeller is driven by a gas turbine. The air passing through the propeller is not heated, so the hot exhaust from the turbine constitutes the primary source of buoyancy. The heat ejected by the turbine can be estimated if the compression ratio of the compressor in the turbine, *CR*,[2] is specified. The compression ratio is the ratio of the stagnation pressures at the outlet and inlet of the compressor.

For an ideal turbine, *CR*, determines the thermal efficiency of the turbine, which is given by

$$\eta_t = 1 - \frac{1}{\alpha_1}$$
$$\alpha_1 = CR^{\frac{k-1}{k}}, \quad (16)$$

where $k = \frac{C_p}{C_v} = 1.4$ is the ratio of the specific heats of air at constant pressure and volume. Then, the power transferred to the propeller is $W = \dot{m}_f H_f \eta_t$ and the heat rejected is

$$Q_e = \dot{m}_f H_f (1 - \eta_t) = \frac{\dot{m}_f H_f}{\alpha_1}, \quad (17)$$

where H_f is the heating value of the fuel, and $\dot{m}_f$is the fuel rate.

The temperature of the exhaust is seen to be

$$T_e = T_a + \frac{H_f}{\alpha_1 C_p AF}, \quad (18)$$

where AF is the air-fuel ratio. This temperature is used to compute the density assuming that the pressure is ambient, p_a,

$$\rho_e = \frac{p_a}{R_a T_e}. \quad (19)$$

This density is used in the formula for the buoyancy parameter equation 3.

The formulation for the buoyancy parameter of the exhaust of a piston engine is similar to that of a turbine. Here the compression is defined in terms of volumes of the fuel-air mixture before and after compression in the engine. The ideal thermal efficiency is given by

$$\eta_t = 1 - \frac{1}{\beta_1}$$
$$\beta_1 = CR^{k-1}. \quad (20)$$

The exhaust temperature used to compute exhaust density becomes

$$T_e = T_a + \frac{H_f}{\beta_1 C_v AF}, \quad (21)$$

where $C_v = C_p/k$ is the specific heat of air at constant volume. Equations (17), (19), and (3) also hold for piston engines, given Equations (20) and (21).

If the power output of the engine is available, we can estimate the thermal efficiency directly as

$$\eta_t = \frac{p_s P_r}{\dot{m}_f H_f}, \quad (22)$$

where p_s is the power setting and P_r is the rated power. Then, the rejected heat, Q_e, is simply

$$Q_e = (1 - \eta_t)\dot{m}_f H_f, \quad (23)$$

[2] UNC needs CR (if applicable) otherwise related power by engine type as input from AEDT from plume rise calculations

as in Equation (17).

The exit temperature, T_e, required to compute the exit density ρ_e(equation 19), is estimated from

$$T_e = T_a + \frac{(1-\eta_t)H_f}{C_p AF}. \quad (24)$$

Now we can calculate the buoyancy parameter F_b from Equation (3).

Note: If we can obtain the rated power directly as an input, there is no need for compression ratio (*CR*) or thermal efficiency as inputs for this category because the related power and power setting are used to calculate the thermal efficiency in Equation (22). Now, we need only one extra column of related power (kilowatt) rather than earlier implemented six engine parameter columns in the AERMOD's HRE file, whereas the power setting values can be used on the basis of air-fuel ratio (AFR) column (Table 1) (Wayson et al., 2009).

Table 4. Representative air-fuel ratios (AFR) by power setting (Wayson et al., 2009).

Mode	Power Setting (%)	AFR
Idle	7	106
Approach	30	83
Climb-out	85	51
Take-off	100	45

Once the buoyancy parameter, F_b, for any category described above is computed, estimating buoyant plume rise from Equation (1) is straightforward.

Exhaust gases exit from jet/gas turbine engines with large horizontal momentum (only for category 1; category 2 does not have the momentum part) and buoyancy. We have a limited understanding of the behavior of such plumes in the atmosphere. The model formulated by Barrett et al. (2013) includes the combined effects of plume buoyancy and horizontal momentum. However, the model has not been evaluated sufficiently to warrant adopting it in preference to the simpler approach, in which total plume rise is the sum of plume rises associated with momentum and buoyancy; the advantage of this approach is that it reduces to well-worn formulations when either buoyancy or horizontal momentum can be neglected. Here we assume that plume buoyancy and momentum act independently, as in Yamartino & Donald (1979), but we allow interaction between these processes as described below.

2.1.3 Accounting for Jet Momentum (Category 1)

We assume that the horizontal momentum is conserved as the radius of the horizontal plume grows with distance from a stationary point within the area source. For a top-hat profile of velocity within the plume, the momentum balance can be written as

$$\rho_p U_p (U_p - U_a)\pi r^2 = T, \quad (25)$$

where U_p is the velocity inside the plume *relative to a stationary observer*, U_a is the ambient velocity at the level of the plume, and ρ_p is the plume density. The initial momentum flow inside the plume is the thrust, T, exerted by the engine on the air. A version of this equation is derived in Appendix A1 of Arunachalam et al. (2017a).

As in Barrett et al. (2013), we assume that the radius of the jet exhaust grows linearly with distance from a point within the area source:

$$r = \alpha x + r_0, \quad (26)$$

where $\alpha = 0.1$ is an entrainment constant, and r_0 is the radius of the engine exhaust. This estimate of the radius of the plume allows us to calculate the velocity of air, U_p, inside the plume from Equation (22):

$$U_p = U_a \left[0.5 + 0.5\left(1 + \frac{4T}{\pi r^2 \rho U_a^2}\right)^{1/2}\right]. \quad (27)$$

The radius of the momentum plume is taken to grow until the difference between the plume and ambient velocities is comparable to the standard deviation of the ambient horizontal velocity fluctuations, $\sigma_u = 2.0u_*$, where u_* is the surface friction velocity. Then, the maximum plume radius is given by the relationship

$$T = \pi \rho_a r_m^2 (U_a + \sigma_u)\sigma_u, \quad (28)$$

where U_a is evaluated at $z = r_m$, and ρ_a is the ambient density. Then, r_m is given by

$$r_m = \left(\frac{T}{\pi\rho_a(U_a+\sigma_u)\sigma_u}\right)^{1/2}. \quad (29)$$

The plume rise associated with momentum, h_{pm}, is taken to be the radius of the plume

$$h_{pm} = \begin{cases} r_0 + \alpha x, & x \le x_m \\ r_m, & x > x_m \end{cases} \quad (30)$$

where x_m is the distance at which the radius reaches its maximum value:

$$x_m = \frac{(r_m - r_0)}{\alpha}. \quad (31)$$

The effect of buoyancy is treated by assuming that it acts independently on the expanding jet plume.

2.1.4 Plume Rise Due to Buoyancy

We estimate plume rise associated with buoyancy using the formulation applicable to point releases in a neutral atmosphere (Briggs, 1965):

$$h_{pb} = \left(\left(\frac{R}{\beta}\right)^3 + \frac{3}{2\beta^2}\frac{F_b}{U_{eff}^3}x^2\right)^{1/3} - \left(\frac{R}{\beta}\right), \quad (32)$$

where $\beta = 0.6$ is an entrainment constant, x is the effective distance between the area source and receptor, and U_{eff} is the effective velocity, which is taken to be the maximum of the velocity in the jet, U_p, and the ambient velocity at plume height, U_a.

Buoyant plume rise interacts with that associated with horizontal momentum through the initial radius, R, in Equation (32). It is taken to be the average value of the radius of the momentum plume between 0 and x to account for the impact of momentum on the initial radius of the buoyant plume,

$$R = \frac{1}{x}\int_0^x r(x)\,dx, \quad (33)$$

which yields

$$R = \begin{cases} r_0 + \alpha x/2, & x \le x_m \\ \frac{x_m}{x}\left(r_0 + \frac{\alpha x_m}{2}\right) + r_m\left(1 - \frac{x_m}{x}\right), & x > x_m \end{cases} \quad (34)$$

The buoyancy parameter, F_b, is computed using the equations described previously. Equation (32) has to be solved iteratively because wind speed at plume height is not known a priori.

The total plume rise is then

$$h_p = h_{pb} + h_{pm}, \quad (35)$$

where the second term on the right-hand side is the plume rise associated with the momentum jet, given by Equation (30) only for category 1; for category 2, it is almost negligible or zero.

2.1.5 Buoyancy Flux and Plume Rise Results

In this section, we present the results of buoyancy flux and plume rise for one day of summer 2012 (July 1, 2012) at LAX. For this day, there was no climb-out source up to 22 m height. All engine parameters were taken from the sample AERMOD HRE plume rise files, which UNC obtained from Volpe.

2.1.5.1 Buoyancy Flux

Here, we plot the buoyancy flux with respect to fuel burn rate; the color bar represents the thrust for surface and airborne sources for both types of aircraft engines (Figures 12 and 13).

2.1.5.1.1 Surface Aircraft Sources

Here, we calculated the buoyancy flux for all sources having 12 m height, especially all surface take-off sources only (surface aircraft sources) in all 24 hours of a day for both types of engines. We found that turbofan engines have much larger buoyancy flux than shaft-based engines and that the number of shaft-based engines is less compared to turbofan engines (Figure 12). Overall, the higher the fuel burn rate, the higher the buoyancy flux.

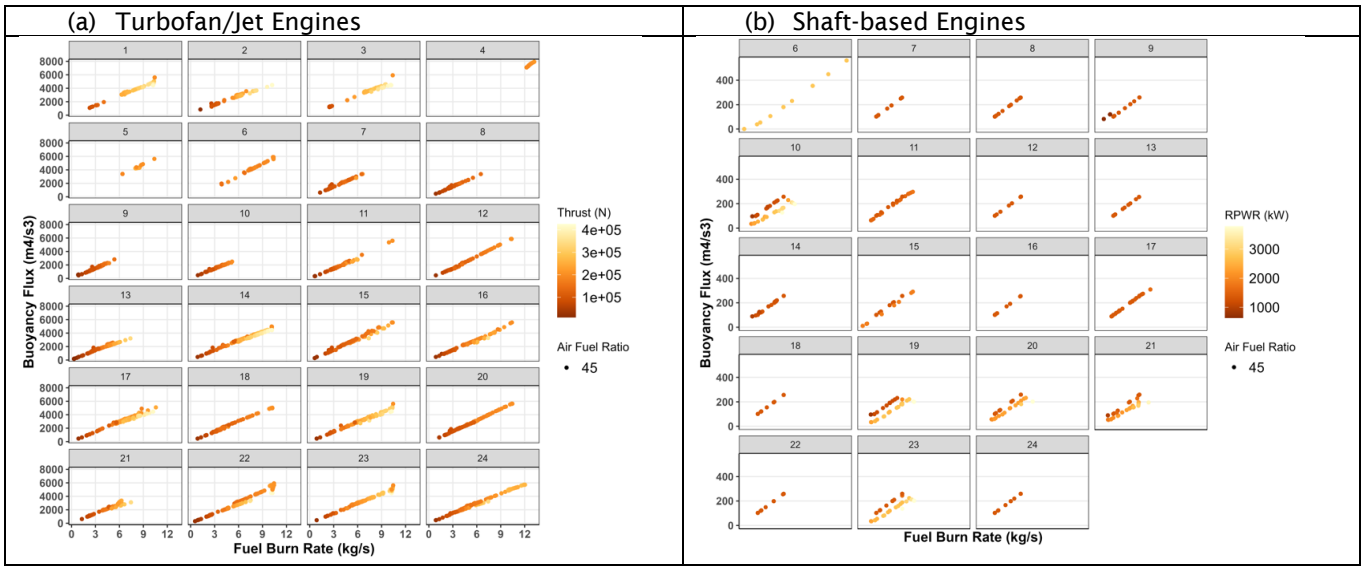

Figure 12. Buoyancy flux with respect to fuel burn rate for (a) turbofan, and (b) shaft-based aircraft engines for surface sources at 12 m height.

2.1.5.1.2 Airborne Aircraft Sources

Here, we show the buoyancy flux for airborne sources at 22 m height only and found that turbofan engines have higher buoyancy flux than shaft-based engines at each hour (Figure 13).

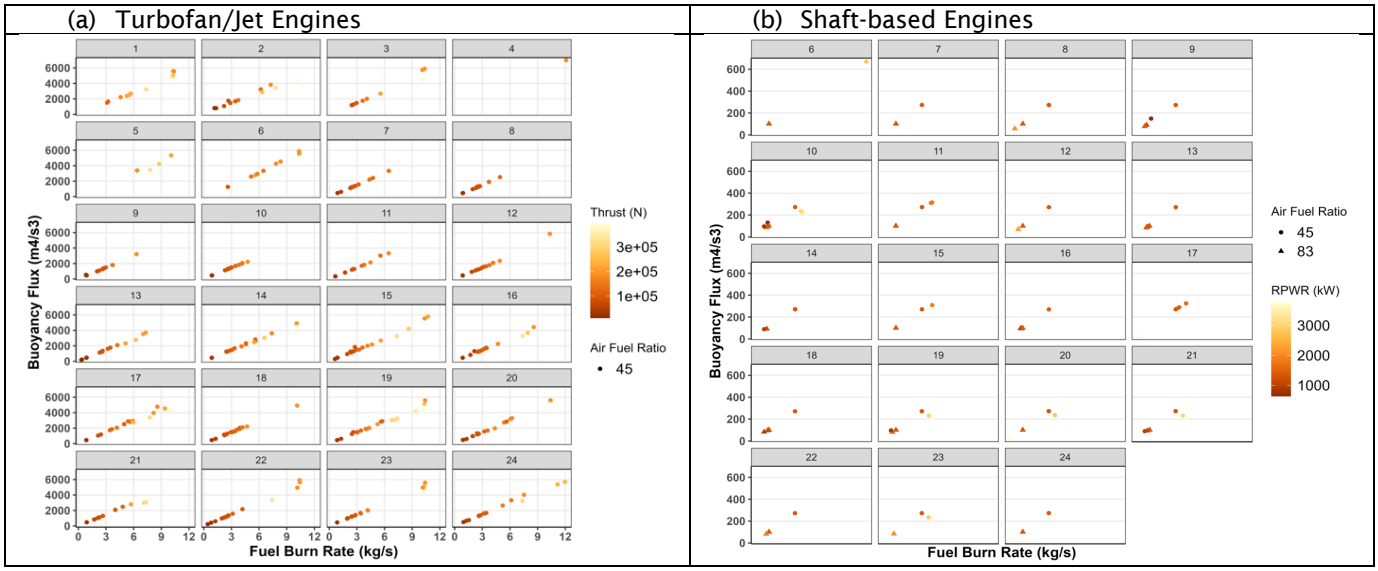

Figure 13. Buoyancy flux with respect to fuel burn rate for (a) turbofan, and (b) shaft-based aircraft engines for airborne sources at 22 m height.

2.1.5.2 Plume Rise

Here, we calculate the plume rise at 100 m downwind from the sources for both type of engines at each mode (Figures 14 and 15).

2.1.5.2.1 Surface Aircraft Sources

For surface sources, the maximum plume rise at 100 m downwind distance is about 30 m for turbofan/jet engines and around 120 m for shaft-based engines.

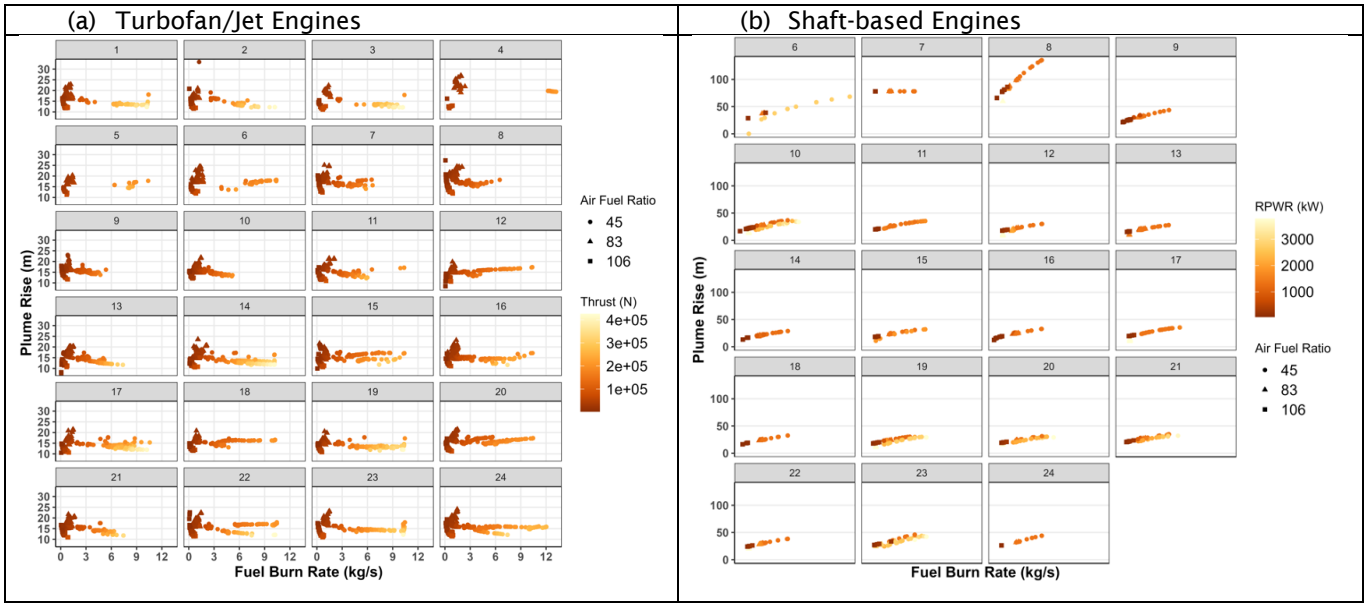

Figure 14. Plume rise with respect to fuel burn rate for (a) turbofan, and (b) shaft-based aircraft engines for airborne sources at 12 m height at each landing/take-off (LTO) mode.

2.1.5.2.2 Airborne Aircraft Sources

For airborne sources, the maximum plume rise at 100 m downwind distance was about 180 m for turbofan/jet engines and around 150 m for shaft-based engines.

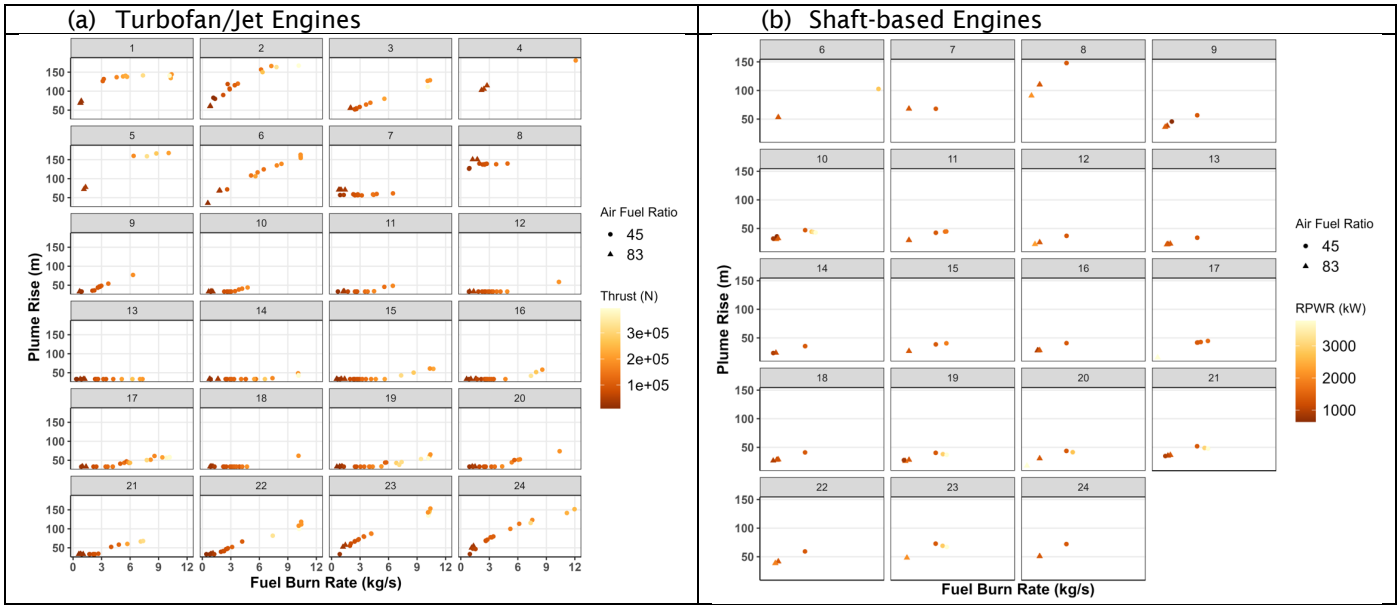

Figure 15. Plume rise with respect to fuel burn rate for (a) turbofan, and (b) shaft-based aircraft engines for airborne sources at 22 m height at each landing/take-off (LTO) mode.

2.1.6 Meteorological Modifications in AERMET-Generated Output Files

Modeling dispersion of aircraft-related sources poses challenges because of the large number and variety of airport sources, which include aircraft, ground operation vehicles, and traffic in and out of the airport, most of which are mobile. Emissions from aircraft sources are transient, buoyant, and occur at different heights from the ground. Quantifying these emissions and modeling the governing processes is challenging. An added complexity occurs when the airport is situated near a shoreline, where meteorological conditions are far from being spatially uniform. These features that characterize the dispersion of airport emissions are being incorporated into the AERMOD model in this work. This work examines the impact of shoreline meteorology and urban effects on dispersion by comparing model estimates of SO_2 with corresponding measurements made during a field study conducted at LAX during winter and summer of 2012 at the four core sites (AQ, CN, CE, and CS) as part of the LAX AQSAS. We modified the output from AERMOD's meteorological preprocessor AERMET to account for (a) the formation of the internal boundary layer that is formed when stable air from the ocean flows onto the warmer land surface of the airport, and (b) urban roughness effects on winds flowing from Los Angeles, east of the airport. Simulations with unmodified AERMET yielded concentrations that were substantially higher than the concentrations at AQ and CS and much lower than those at CN and CE. Model performance improved when AERMOD used modified meteorology. The fraction of model estimates within a factor of 2 of the observations (FAC2) improved from 0 to 31% at the CS and CE sites by up to 50% in winter season, whereas in summer, FAC2 improved only at the CE site. The ratio of robust highest modeled value to measured value improved from 7.72 to 2.78 and from 4.92 to 1.94, respectively, in winter and summer seasons. Overall, in the morning and late evening hours, concentrations are decreasing with modified met (Figure 16).

This meteorological modification work has been accepted for publication in the *Atmospheric Environment* journal.

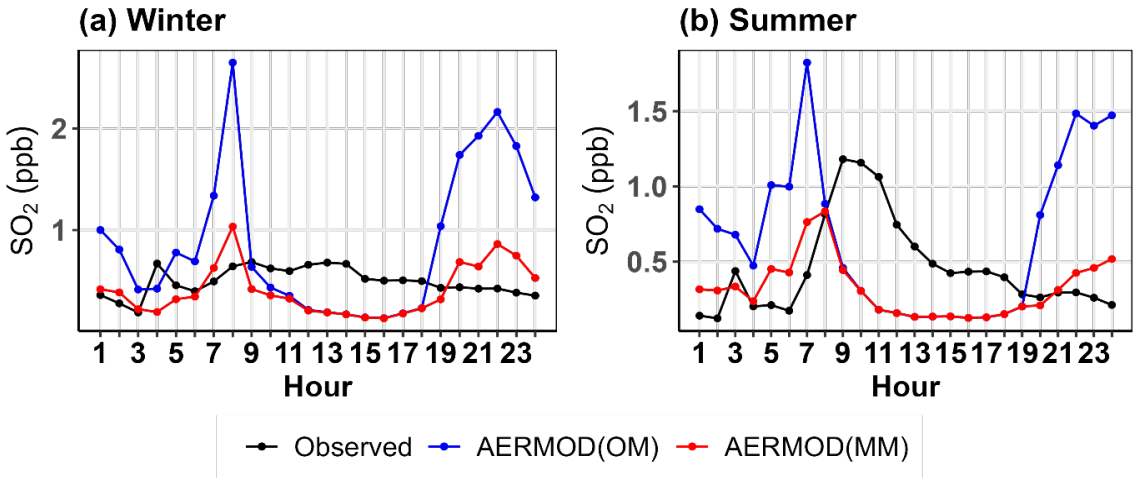

Figure 16. Diurnal variation of SO_2 concentrations averaged over the four sites and experimental periods.

3. Chemical Processes

AERMOD greatly underpredicted the NO_2 concentrations using all its chemistry schemes, which was due to the lack of chemical reactions. More detailed chemistry schemes can improve the estimation of NO_2 concentrations. ADM is a decoupled model, where the dispersion module first estimates the NOx and volatile organic compound (VOC) concentrations at each of the receptors along with "Age," the time it takes to reach the receptor from the source. ADM chemistry uses these concentrations as initial concentrations and Age as time to solve differential chemistry equations for NO_2 and PM. Addition of VOC speciation using Wilkerson et al. (2010) did not greatly improve the NO_2 concentrations.

In ADM, NO_x-NO_2 conversion can be modeled using four different schemes: ozone limiting method (OLM) based on Cole and Summerhays (1979), travel time method (TTM) based on AERMOD's travel time reaction method (TTRM), generic reaction set (GRS) based on Venkatram et al. (1994), and ambient ratio method (ARM) based on AERMOD's ARM2. Although NO_2 contributions by LTO operations at each receptor are estimated for both summer and winter periods, only summer results are used for model evaluation.

Model performance was compared against observations after adding the NO_x concentrations from AERMOD (with non-LTO emissions) to ADM-dispersion outputs. OLM performed slightly better than the other three schemes, followed by TTRM, GRS, and ARM. The ADM results for NO_2 concentrations contributed by LTO operations can be seen in Figure 17. To evaluate model performance, the ADM results from all operations near LAX can be seen in Figure 18, and the evaluation metrics for different schemes can be found in Table 5.

Diurnal Concentration Distribution

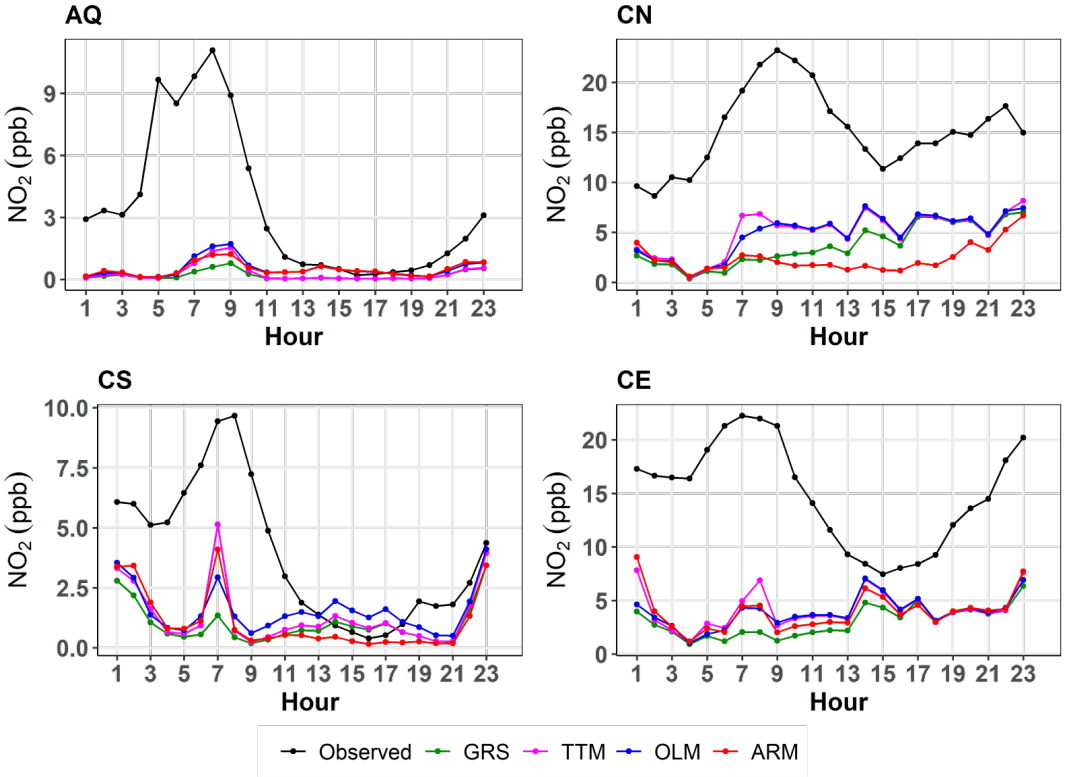

Figure 17. Diurnal variability in observed and modeled NO_2 concentrations for the summer period at all four core sites (AQ, CN, CS, and CE) contributed by the landing/take-off (LTO) operations at LAX. GRS, generic reaction set; TTM, travel time method; OLM, ozone limiting method; ARM, ambient ratio method.

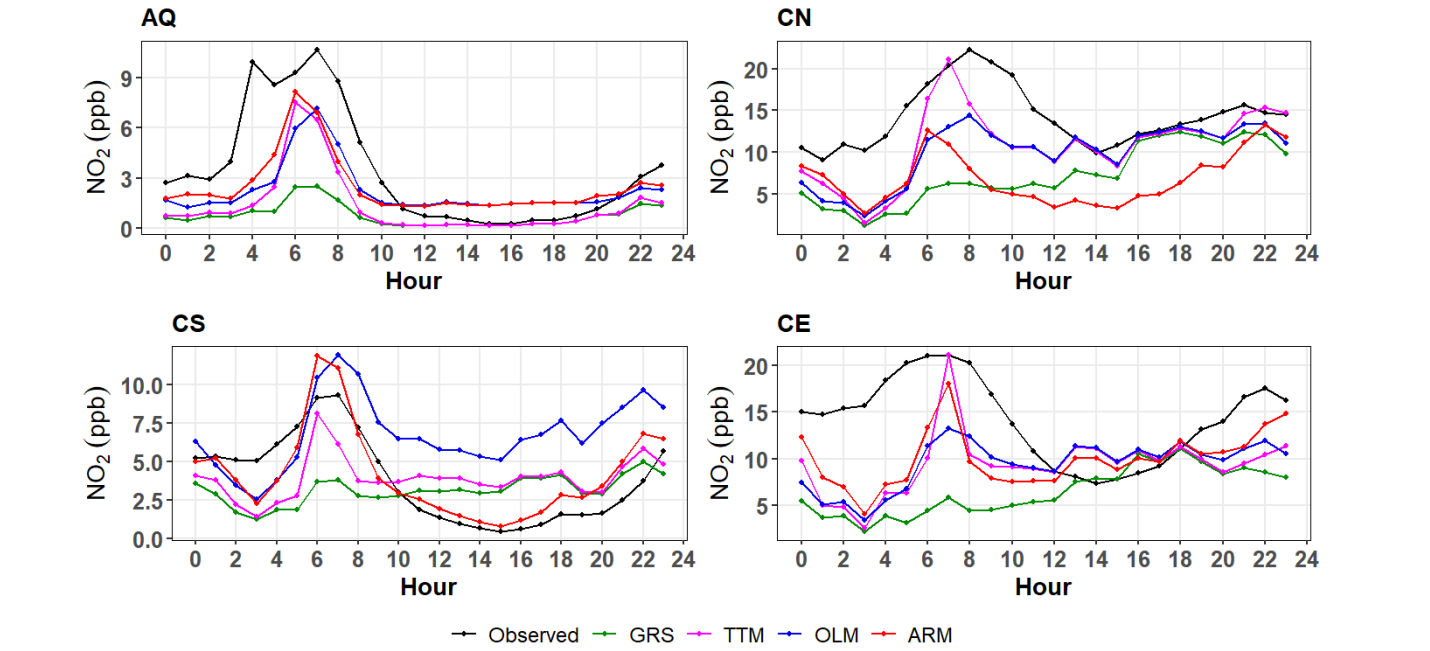

Figure 18. Diurnal variability in observed and modeled NO_2 concentrations for summer period at all four core sites (AQ, CN, CS, and CE) contributed by the landing/take-off (LTO) operations modeled by LAX and the rest of the emissions modeled by AERMOD. The evaluation metrics for each of these schemes can be found in Table 5. GRS, generic reaction set; TTM, travel time method; OLM, ozone limiting method; ARM, ambient ratio method.

Table 5. Evaluation metrics for different ADM chemistry schemes. GRS, generic reaction set; TTM, travel time method; OLM, ozone limiting method; ARM, ambient ratio method[3].

	FAC2	R2	FB	IOA	AFB_RHC
GRS	0.33	0.44	0.68	0.56	0.38
TTM	0.39	0.49	0.33	0.59	-0.9
OLM	0.45	0.47	0.22	0.59	0.31
ARM	0.48	0.37	0.44	0.57	-0.62

From the results, CN and CE were the most affected among the four sites due to aircraft LTO operations. ADM estimated that LTO operations contributed, on average, 4.90 and 3.54 ppb/hour of NO_2 at the sites CN and CE, respectively. These values are comparable with those of Carslaw et al. (2006); they estimated upper limit of NO_2 contribution as 7.98, 3.51, 3.46, 2.23, 1.06, 0.8, and 0.8 ppb at seven receptors using 2001–2004 data.

We also coded for modified GRS (MGRS) based on Venkatram et al. (1997) but are still determining the initial concentrations for other chemical compounds involved in this scheme. Initial results for MGRS can be seen in Figure 19, where the initial concentrations of compounds other than NO and NO_2 are assumed as ROC1 = 0.5*ROG; AROM=0.5*ROG; TERP=0; aH2O2=0; RNO3=0; OH=10; SO4=0; HNO3=0; y1_OC=0; y2_OC=0; SO2=0. The underestimation of NO_2 could be due to lower VOC concentrations or due to the conversion of NO_2 to HNO_3. [ROC: Reactive Organic Compounds; ROG: Reactive Organic Gases;

[3] FAC2: Factor of two; R2: R-squared; FB: Fractional Bias; IOA: Index of Agreement; AFB_RHC: Fractional Bias for Robust Highest Concentrations

AROM: Aromatics; TERP: Terpenes; H2O2: Hydrogen Peroxide; RNO3: Radical Nitrate; SO4: Sulfate; HNO3: Nitric Acid; OC: Organic Carbon; SO2: Sulfur dioxide; NO; Nitrogen oxide; NO2: Nitrogen dioxide]

Diurnal Concentration Distribution

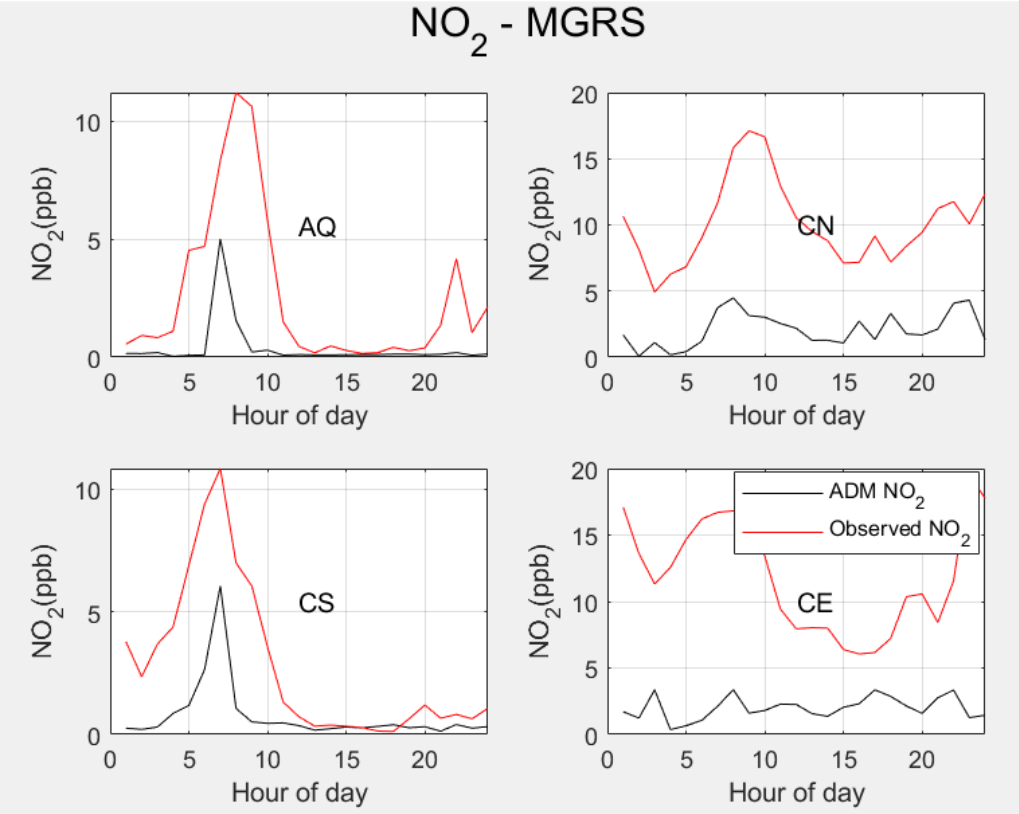

Figure 19. Diurnal variability in observed and modeled NO_2 concentrations for the first 5 days of summer at the four core sites (AQ, CN, CS, and CE) contributed by landing/take-off (LTO) operations at LAX.

4. Model Evaluation

4.1 ADM Evaluation With and Without Plume Rise

The newly developed ADM was evaluated using the SO_2 measurements from the Los Angeles AQSAS for both seasons (winter and summer of 2012). In the past year, we updated the ADM and added some additional features, including meander for low wind dispersion. Here, we present only the diurnal concentration distributions for both seasons. We found that the higher concentrations decreased and came close to the diurnal observed concentrations at all four core sites (AQ, CN, CS, and CE) using the plume rise algorithm and the meander algorithm with ADM in both seasons of 2012 (Figure 20). However, here, we modeled only the aircraft emissions.

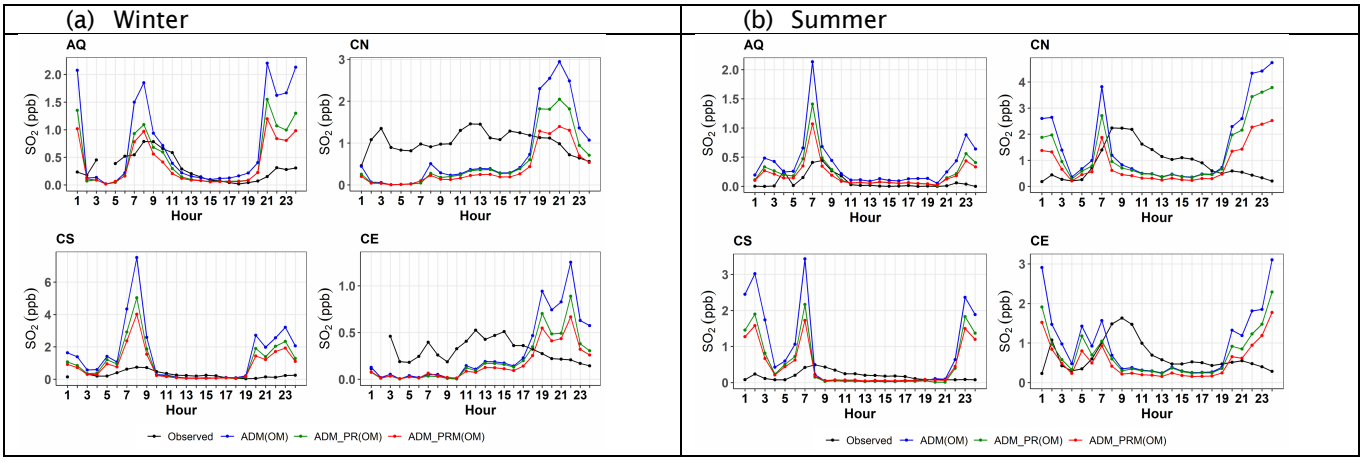

Figure 20. Diurnal variation of SO_2 concentrations at the four core sites (AQ, CN, CS, and CE).

4.2 AERMOD Evaluation With and Without Plume Rise for Both Source Types (AREA and VOLUME)

We evaluated updated AERMOD having plume rise using NOx observed concentrations for both source types only in summer of 2012. Here, we used only the emissions from aircraft sources. We found that the high concentrations decreased substantially for source types with plume rise (Figures 21 and 22).

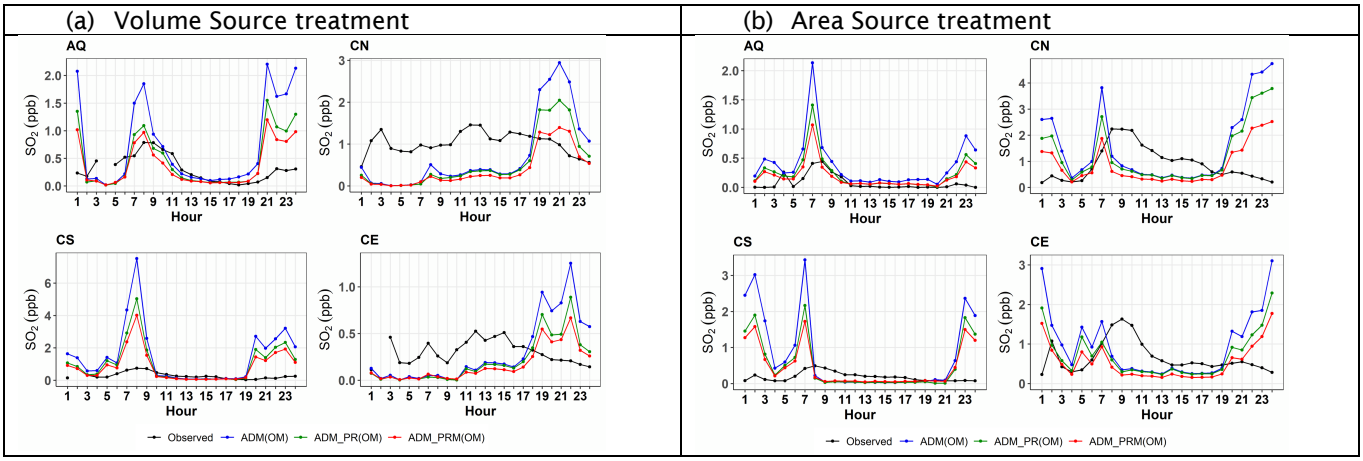

Figure 21. Diurnal variation of NO_x modeled and observed concentrations at the four core sites (AQ, CN, CS, and CE).

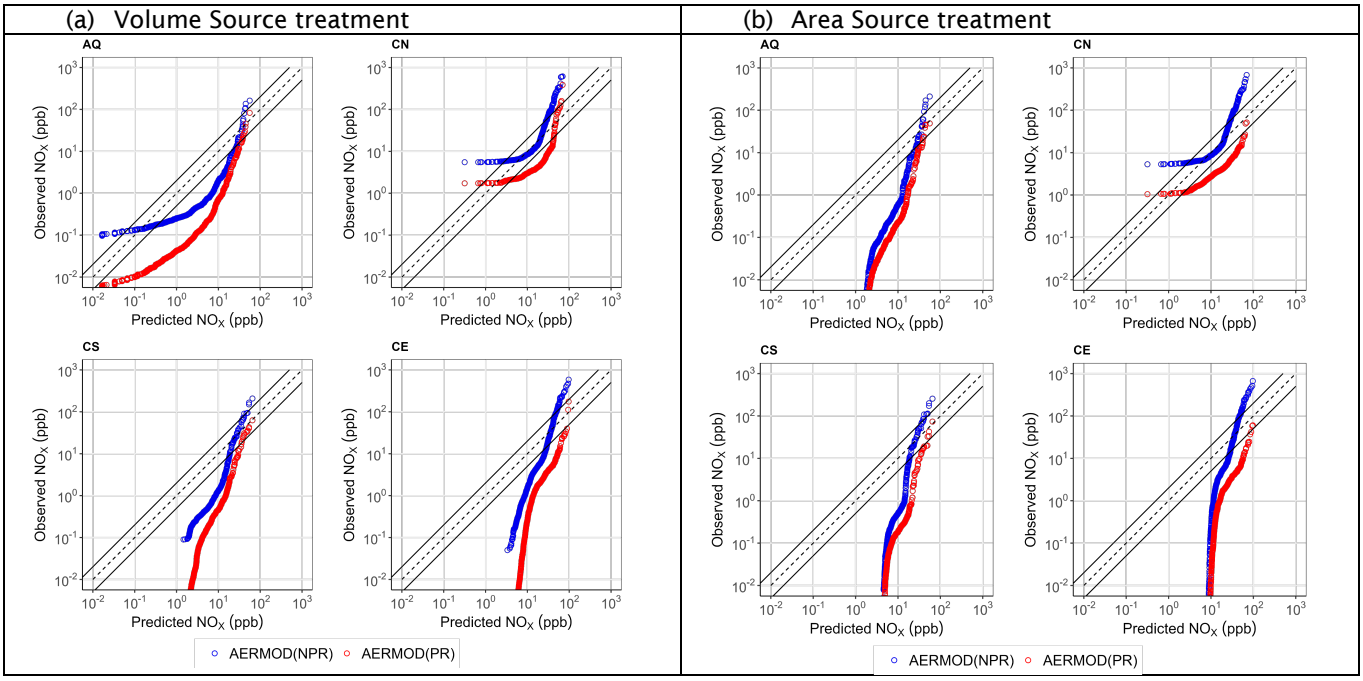

Figure 22. Quantile-quantile (QQ) distribution of NO_x modeled concentrations with respect to observed concentrations at the four core sites (AQ, CN, CS, and CE).

5. Preparing AEDT Emissions Inventories

UNC was involved in all AEDT updates to generate the AERMOD-ready inputs for aircraft plume rise. For this, UNC developed a plume rise algorithm for both types of aircraft engines (turbofan/jet and shaft-based engines). During this development, we found that the jet engine's buoyancy flux computation, the heat rejection term became negative. To overcome this, UNC developed another method to compute heat rejection for turbofan/jet engines, which is based on the Mach number but as per the Volpe team, this algorithm was not working for high bypass ratio. After this, we agreed to use the first algorithm, which gives negative heat rejection for inconsistent fuel burn rate and thrust values. We are now ignoring records with negative heat rejection hours/sources. Based on the plume rise parameters file exchange and analysis of those files, UNC performed many statistical analyses of the algorithm and files. UNC also developed two different approaches to compute the buoyancy flux for shaft-based engines, one based on the compression ratio and the other on the rated power. The first method was not applicable to introduce within AEDT, as compression ratio was not available. Based on this work, the Volpe team updated the AEDT model to generate AERMOD-ready input files as well as files for AEDT2ADM.

Task 2: Develop and Evaluate a Multiscale WRF-SMOKE-CMAQ Model Application for BOS Focused on UFP

1. CMAQ Application for BOS

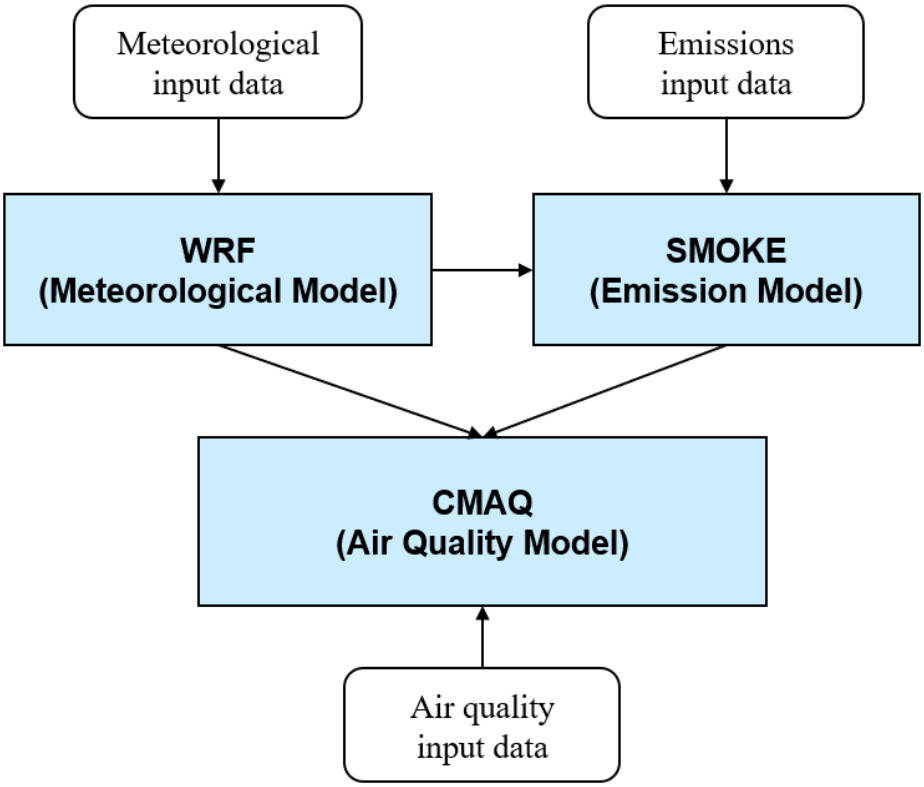

Figure 23. Weather Research and Forecasting–Sparse Matrix Operator Kernel Emissions–Community Multiscale Air Quality Model (WRF-SMOKE-CMAQ) modeling system.

1.1 Weather Research and Forecasting (WRF)
Weather Research and Forecasting (WRF) was developed by the National Center for Atmospheric Research (NCAR) and the National Center for Environmental Prediction (NCEP) in the National Oceanic and Atmospheric Administration (NOAA). It is a meteorological model using fully compressible non-integer equations, and the horizontal grid utilizes the Arakawa-c grid system and uses the hydrostatic barometric pressure vertical coordinates based on topography. The WRF modeling software consists of a dynamic processing module (ARW solver) including preprocessing, bidirectional and unidirectional nesting, and various post-processing programs.

1.2 Community Multiscale Air Quality Model (CMAQ)
The CMAQ modeling system is currently widely used in various fields by many researchers worldwide. The preprocessors of CMAQ are ICON (Initial CONditions processor), which is an initial condition generation module, BCON (Boundary CONditions processor), which is a boundary condition generation module, MCIP (Meteorology-Chemistry Interface Processor), which is in charge of preprocessing meteorological data, and a chemical transport module, which is composed of CCTM (Chemical Transport Model). Using the results derived through the preprocessing module as input data, CCTM numerically calculates the 3D advection diffusion equation to calculate the concentration of pollutants in space every hour. At this time, horizontal and vertical advection, horizontal and vertical diffusion, deposition, and gaseous chemical reactions, etc. applied to the law of conservation of mass in the advection process are considered.

1.3 Comparison of Base-NEI 2017 (2017 National Emission Inventory [NEI]) and No-Airport (NEI Without Airport Emission)

CMAQ was used to evaluate the impact of airport emissions with configuration in Table 6 for winter (January) and summer (July) 2017.

Table 6. CMAQ v5.3.3 model configuration.

	Domain 1	Domain 2	Domain 3
Horizontal Grid	459 × 299 (12US2)	102 × 108	126 × 141
Resolution (km)	12 km × 12 km	4 km × 4 km	1.33 km × 1.33 km
Vertical Grid	35 Layers		
CMAQ Chemical Option	· Carbon Bond 6 r3 · AERO 6 non-volatile POA (6th generation CMAQ aerosol module)		
SMOKE Input Data	· NEI 2017 Emission		
Modeling Period	January 1-31, 2017	July 1-31, 2017	
	2-week spin-up in Dec 2016	2-week spin-up in June 2017	

1.4 $PM_{2.5}$ Monthly Average

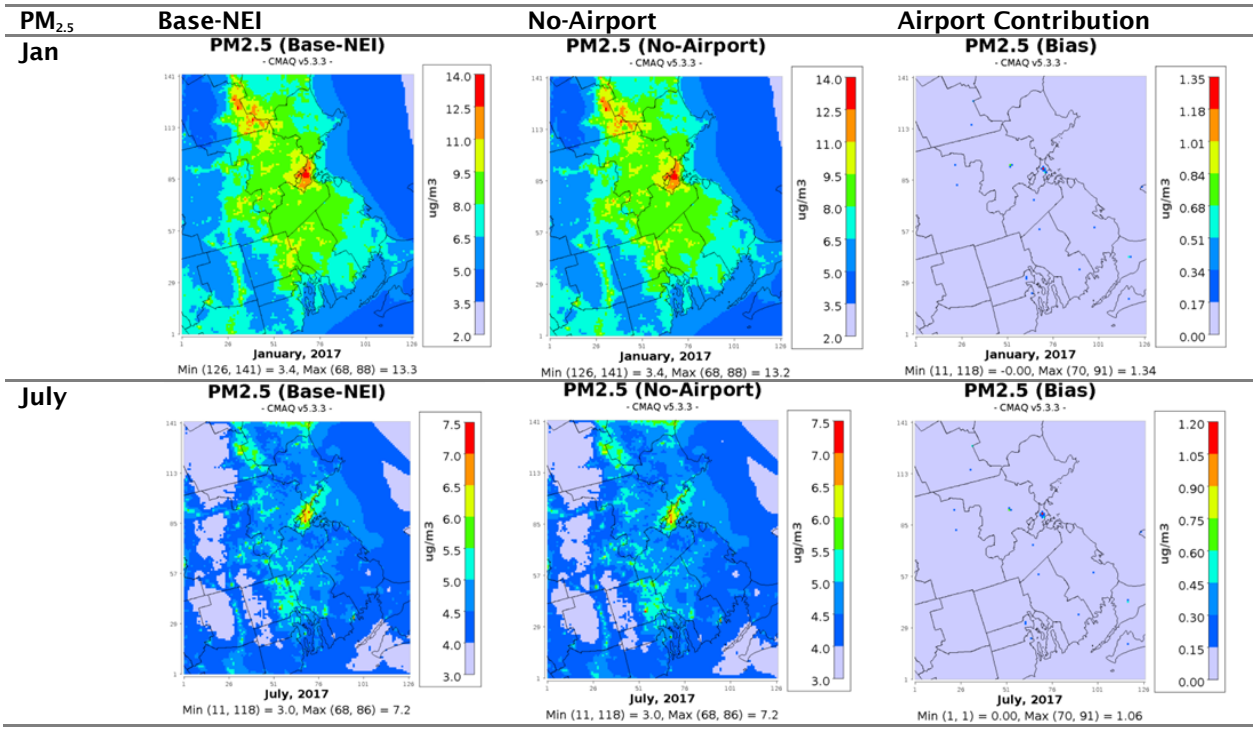

Figure 24. Comparing Base-NEI and No-Airport with $PM_{2.5}$ (monthly average) for January and July (1.33 km × 1.33 km).

CMAQ modeling of $PM_{2.5}$ monthly average concentration for January 2017 demonstrated a 10.7% reduction in $PM_{2.5}$ concentration (from 12.5 to 11.2 μg/m^3) at Airport grid-cell (70, 91), showing the maximum reduction. For July 2017, although the absolute concentration reduction and maximum concentration were low, the 15.1% reduction in $PM_{2.5}$ (from 7.0 to 6.0 μg/m^3) showed that the contribution of airport emission to $PM_{2.5}$ was higher in July than in January.

1.5 Maximum Daily Average 8-Hour O_3 Monthly Average

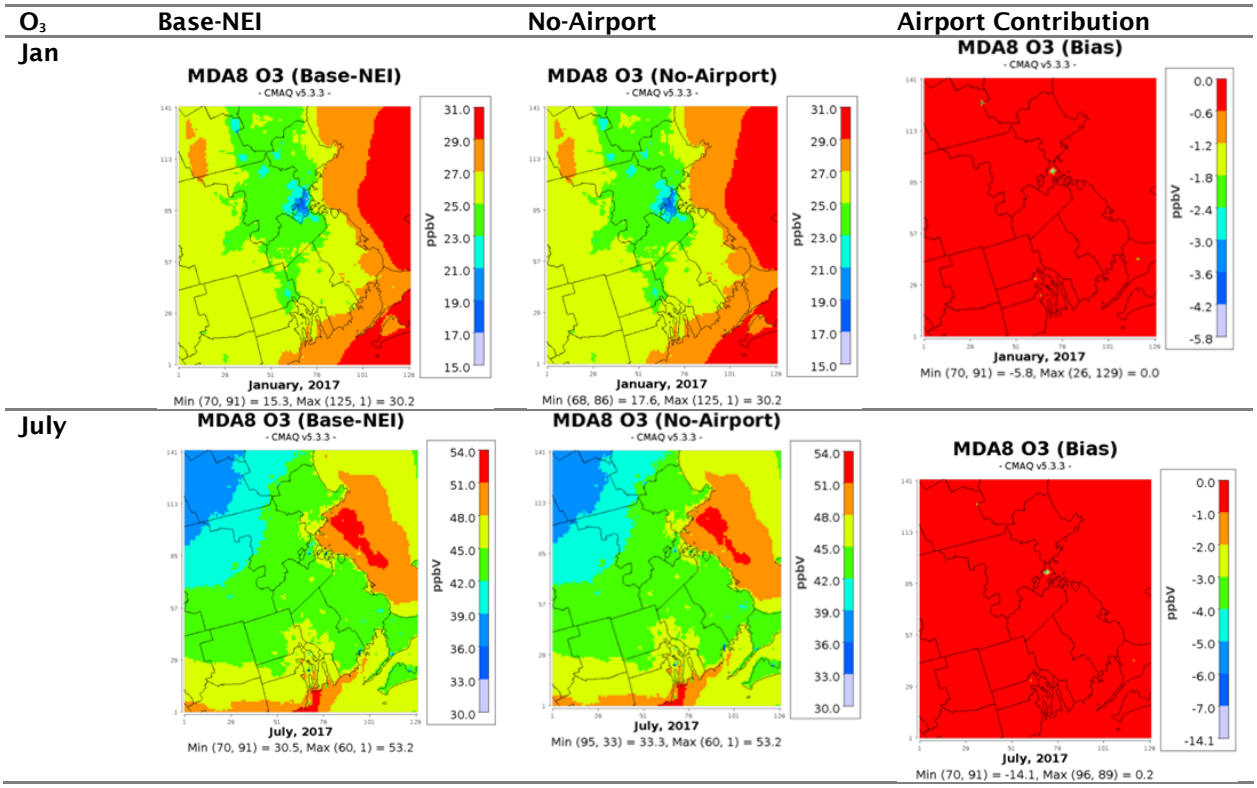

Figure 25. Comparing Base-NEI and No-Airport with O_3 (maximum daily average 8-hour) for January and July (1.33 km × 1.33 km).

In contrast, monthly average of O_3 maximum daily average 8-hour (MDA8 O_3) for January 2017 demonstrated a 37.9% increase in $PM_{2.5}$ concentration (from 15.3 to 21.1 ppb) at Airport grid-cell (70, 91), showing the maximum differences. For July 2017, $PM_{2.5}$ increased 46.2% (from 30.5 to 44.6 ppb), showing that the contribution of airport emission to O_3 (as shown by $PM_{2.5}$ concentration) was higher in July than in January.

1.6 NO_2 Monthly Average by Time

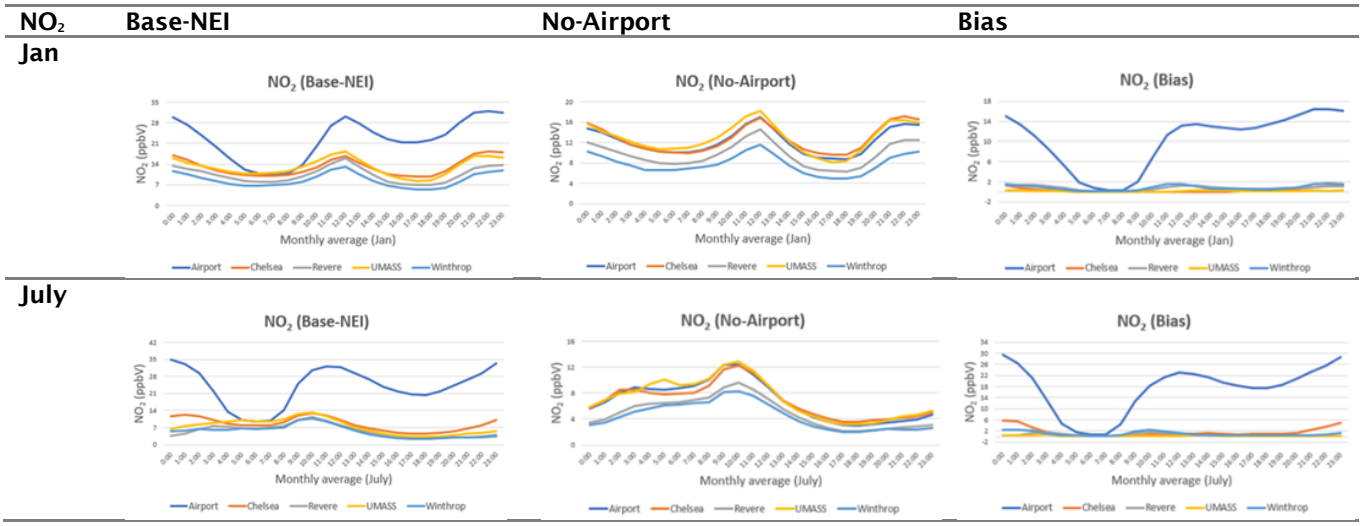

Figure 26. Comparing Base-NEI and No-Airport with NO_2 (monthly average each time) for January and July with airport and four monitoring sites.

In the Base-NEI scenario, NO_2 monthly average concentration by time for January (from 10.4 to 32.0) and July 2017 (from 9.4 to 35.0) showed that NO_2 concentration was highest at the airport except from 5:00 to 7:00 AM because of aircraft activities. In the No-Airport scenarios, however, airports with four monitoring sites, which were the near airport, showed a similar pattern of NO_2 concentrations.

2. Computing Exceedance in the Boston Domain

The Clean Air Act requires EPA to set NAAQS for six principal pollutants ("criteria" air pollutants) that can be harmful to public health and the environment. Units of measure for the standards are parts per million (ppm) by volume, parts per billion (ppb) by volume, and micrograms per cubic meter of air (μg/m^3). CMAQ results are post-processed to evaluate the contribution of airport for criteria pollutants based on NAAQS analyses. Therefore, we computed exceedances in the Boston area (1.33 km domain) by scenarios with different pollutants ($PM_{2.5}$, O_3, and NO_2) for January and July.

2.1. Daily $PM_{2.5}$

In January, 840 grid-cells in the Base-NEI scenario and 822 grid-cells in the No-Airport scenario exceeded 25 μg/m^3 of $PM_{2.5}$, a difference of 18 grid-cells near airports; no grid-cell exceeded more than twice. The number of grid-cells exceeding 30 μg/m^3 of $PM_{2.5}$ was 80 in the Base-NEI scenario and 75 in the No-Airport scenario, a difference of 5 grid-cells, near Manchester-Boston Regional Airport. Even though the highest monthly average $PM_{2.5}$ occurred near BOS, a greater number of exceedances were found near Manchester-Boston Regional Airport. No grid-cells showed $PM_{2.5}$ exceedances of more than 35 μg/m^3. In July, 22 grid-cells exceeded the 25 μg/m^3 of $PM_{2.5}$ concentration in the Base-NEI and No-Airport scenarios (Table 7 and Figure A1).

Table 7. The number of daily $PM_{2.5}$ exceedances in Boston domain by scenario.

Daily $PM_{2.5}$ Scenarios	Exceeded 25 µg/m³	Exceeded 30 µg/m³	Exceeded 35 µg/m³
Base-NEI (Jan)	840	80	7
Base-NEI (Jul)	22	0	0
No-Airport (Jan)	822	75	7
No-Airport (Jul)	22	0	0

2.2 Annual $PM_{2.5}$

A total of 233 grid-cells in the Base-NEI scenario and 221 grid-cells in No-Airport scenario exceeded 8 µg/m³ of $PM_{2.5}$, with eight of these 12 grid-cells near airports. Two and one grid-cells, respectively, exceeded 10 µg/m³ of $PM_{2.5}$ in the Base-NEI and No-Airport scenarios; the only difference was at BOS. No grid-cell showed annual $PM_{2.5}$ exceedances of more than 12 µg/m³ (Table 8 and Figure A2).

Table 8. The number of annual $PM_{2.5}$ exceedances in the Boston domain by scenario.

Annual $PM_{2.5}$ Scenarios	Exceeded 8 µg/m³	Exceeded 10 µg/m³	Exceeded 12 µg/m³
Base-NEI (Jan + Jul)	233	2	0
No-Airport (Jan + Jul)	221	1	0

2.3. Ozone (O_3)

In January, no grid-cells showed O_3 exceedances at any standard (60, 65 70 ppb). In contrast, the July O_3 concentration exceeded 60 ppb at 29,166 grid-cells in the Base-NEI scenario and 28,946 in the No-Airport scenario, showing differences mainly on the East and South coastline. Some grid-cells exceeded 60 ppb on 14 of 31 days. Although the number of grid-cells exceeding 65 ppb decreased by more than half relative to 60 ppb, more than 12,000 grid-cells exceeded 65 ppb in both scenarios. More than 4,684 grid-cells exceeded the O_3 standard (70 ppb) in the Base-NEI scenario. The number exceeding 70 ppb increased near Boston airport (Table 9 and Figure A3).

Table 9. The number of maximum daily average (MDA) 8-hour O_3 exceedances in the Boston domain by scenario.

MDA O_3 Scenarios	Exceeded 60 ppb	Exceeded 65 ppb	Exceeded 70 ppb
Base-NEI (Jan)	0	0	0
Base-NEI (Jul)	29,166	12,508	4684
No-Airport (Jan)	0	0	0
No-Airport (Jul)	28,946	12,324	4638

2.4. Nitrogen Dioxide (NO_2)

A greater number of grid-cells exceeding 5 ppb and 10 ppb were found in the Base-NEI compared with the No-Airport scenario in January and July. The only grid-cells exceeding 20 ppb were for BOS in January and July. No grid-cells exceeded the NO_2 NAAQS standard (53 ppb).

Table 10. The number of NO_2 exceedances in the Boston domain by scenario.

Daily NO_2 Scenarios	Exceeded 5 ppb	Exceeded 10 ppb	Exceeded 20 ppb	Exceeded 53 ppb
Base-NEI (Jan)	4,392	129	1	0
Base-NEI (Jul)	148	15	1	0
No-Airport (Jan)	4,328	122	0	0
No-Airport (Jul)	131	10	0	0

2.5. Particle Number Concentration (PNC)

The ultrafine particle number concentration (UFPNC) was computed based on error function approximation (Jiang et al., 2006; Meng & Seinfeld, 1994). The diameter for UFP in this research was between 7 nm and 100 nm. The UFPNC is the sum of Aitken mode and accumulation mode with their diameter and standard deviation.

Table 11. Calculation of UFP number concentrations.

Variable	Value or Equation
Low diameter cut (LDC)	7 nm
Upper diameter cut (UDC)	100 nm
Aitken mode	
ERF1 Aitken [a, b]	ERF((LOG(LDC) - LOG(DGATKN_WET))/(SQRT * LOG(STDEVATKN)))
ERF2 Aitken	ERF((LOG(UDC) - LOG(DGATKN_WET))/(SQRT * LOG(STDEVATKN)))
fUFP Aitken	0.5*(ERF2_ATKN – ERF1_ATKN)
Aitken UFP number Conc.	NUMATKN * fUFP_ATKN
Accumulation mode	
ERF1_ACC	ERF((LOG(LDC) - LOG(DGACC_WET))/(SQRT * LOG(STDEVACC)))
ERF2_ACC	ERF((LOG(UDC) - LOG(DGACC_WET))/(SQRT * LOG(STDEVACC)))
fUFP_ACC	0.5*(ERF2_ACC – ERF1_ACC)
ACC. UFP number Conc.	NUMATKN * fUFP_ACC
UFP Number	UFP_ATKN + UFP_ACC

[a] ERF, error function approximation (Meng & Seinfeld, 1994), [b] ERF1, ERF2 (Jiang et al., 2006).

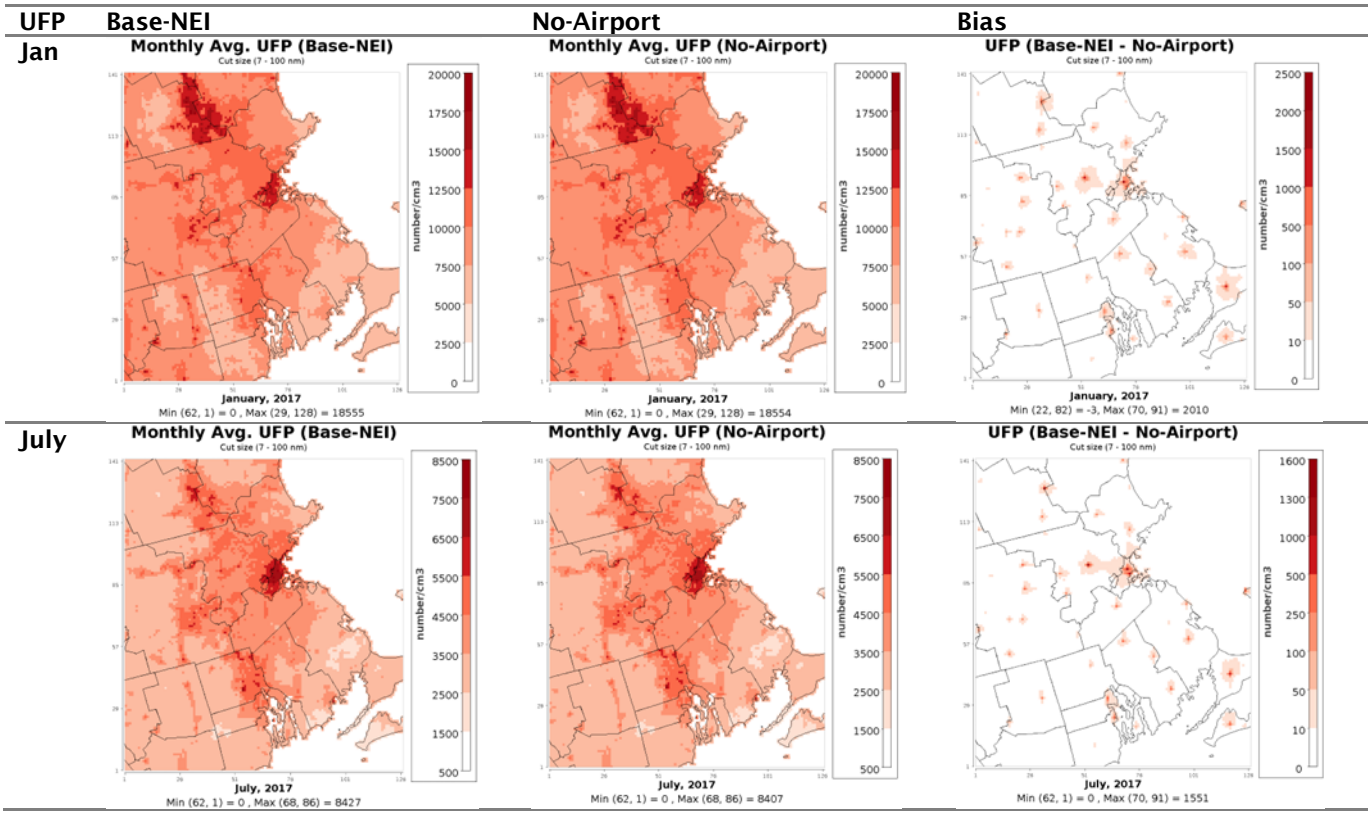

Figure 27. Comparing Base-NEI and No-Airport scenarios with UFP (monthly average) for January and July (1.33 km × 1.33 km).

The monthly average of UFPNC for January 2017 demonstrated that UFPNC decreased by 12.8% (from 15,611 to 13,601 number/cm^3) at airport grid-cell (70, 91) when airport emissions were removed, the maximum reduction. For July 2017, although the absolute concentration reduction and maximum concentration were low, the 19.0% reduction in UFPNC (from 8,157 to 6,606 number/cm^3) showed that the contribution of airport emissions to UFP was higher in July than in January. The contribution of airport emissions to UFP (12.8%, 19.0%) was higher than that to $PM_{2.5}$ (10.7%, 15.1%) for January and July, respectively.

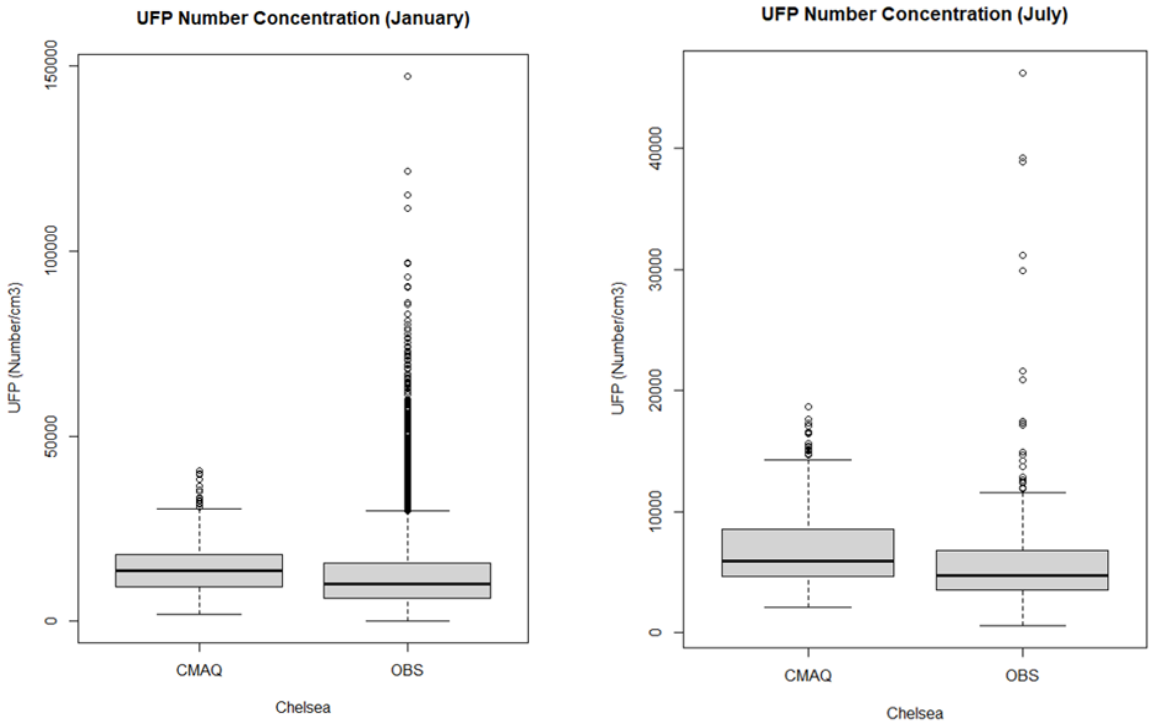

Figure 28. Comparison of CMAQ (Base-NEI) and Observation (OBS) boxplots at Chelsea in January and July.

CMAQ overpredicted the median of observed UFP distribution by 9% for January and by 23% for July but underestimated the 95th percentile by 37% for January and by 3% for July at Chelsea. Furthermore, CMAQ (40,734 number/cm^3) underpredicted the UFPNC by more than half compared with observations (81,101 number/cm^3) at maximum for January. In July, UFPNC showed the same pattern of underprediction between CMAQ (18,683 number/cm^3) and observation (46,230 number/cm^3).

3. Development of AEDT-Based Inventories for BOS

After identifying the basic requirements to run AEDT-3e, we acquired a new desktop server meeting those requirements. We had technical difficulties adding the server to the UNC system and obtaining administrative rights (which are necessary to install AEDT). We successfully installed and ran AEDT-3e for the current IAD Dulles study to obtain dispersion results for NO_2 concentrations at the receptors. The results from the run can be seen in Figure 29.

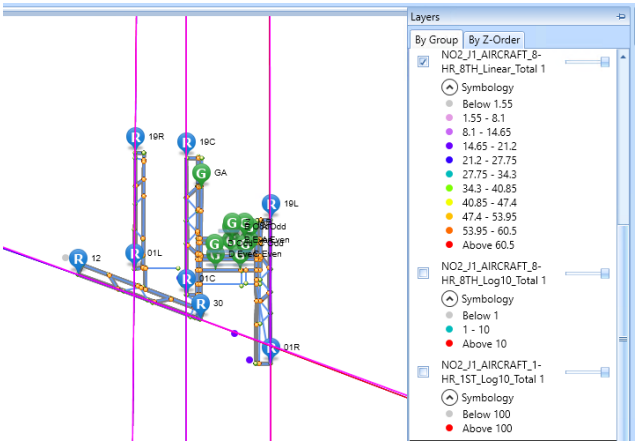

Figure 29. IAD Dulles Airport layout with NO_2 concentrations (in ppb) at the receptors.

Along with the BOS-AEDT study, we are also working on the LAX-AEDT summer 2012 study to replicate the results. SQL-Express could not load a database >10 GB, so we reinstalled AEDT on SQL-Eval 2017 to run the LAX-AEDT test case. The setup for this study can be seen in Figure 30. For AEDT-LAX data, we were able to create seasonal average emission reports.

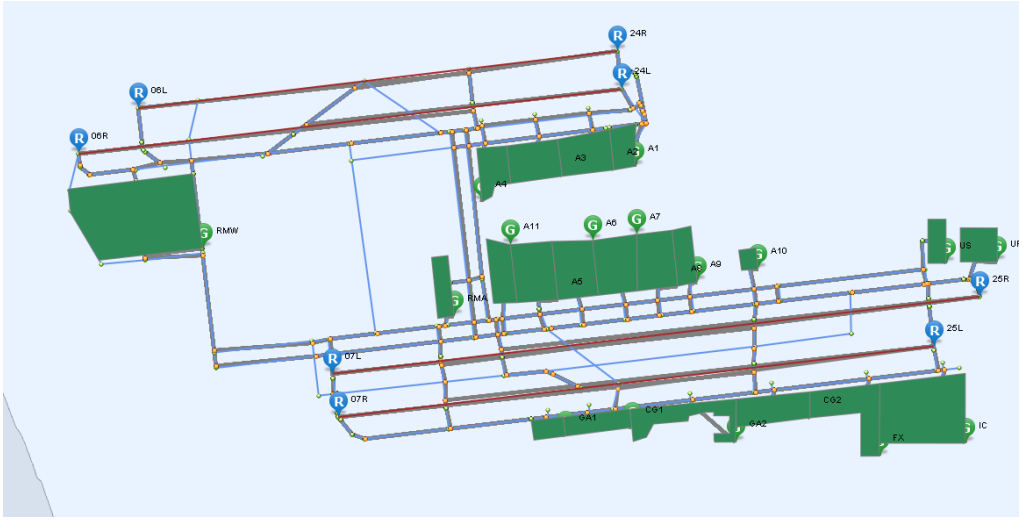

Figure 30. LAX airport layout for summer 2012 study.

We listed the data needed as inputs to run the BOS-AEDT study for 2017. Initially, we only obtained hourly averaged aircraft operational data from BU but later received Performance Data Analysis and Reporting System (PDARS) data. After analyzing it, we highlighted the data gaps for the BOS-AEDT study, which can be found in Appendix Table A1.

Milestones

We submitted drafts of the following documents to the FAA:

- Design document for ADM
- Version 2 of ADM
- Scoping plume Rise treatment document for AEDT/AERMOD plume rise implementation

We also shared the updated AERMOD plume rise implemented version with EPA/FAA.

Major Accomplishments

- Updated design document detailing features that will go into the new ADM
- Developed a scoping document on plume rise treatment with a focus on AERMOD
- Developed a final version of plume rise treatment
- Implemented plume rise in AERMOD and delivered it to the EPA/FAA
- Drafted papers on plume rise algorithm and AREA vs VOLUME source comparison and evaluation of AERMOD at LAX AQSAS

Publications

- Pandey, G., Venkatram, A., & Arunachalam, S. (2022). Evaluating AERMOD with measurements from a major U.S. airport located on a shoreline. *Atmospheric Environment, 294, 119506*. doi:10.1016/j.atmosenv.2022.119506

Outreach Efforts

We presented the ADM work in multiple arenas, including the CMAS 2021 conference held in Chapel Hill (November 2021), the AEC Roadmap meeting held in Washington, DC (May 2022), and the 21st HARMO conference held in Aveiro, Portugal (September 2022).

Awards

None.

Student Involvement

Praful Dodda and Hyeongseok "Darby" Kim are PhD students involved in developing ADM chemistry and the Boston case study, respectively.

Plans for Next Period

- Finalize plume rise implementation in AERMOD and finalize manuscript for submission
- Finalize AEDT data for Boston case study and redo CMAQ modeling using AEDT data for Boston
- Finalize ADM development and evaluate both ADM and AERMOD with LAX AQSAS data

References

Arunachalam, S., Valencia, A., Woody, M., Snyder, M., Huang, J., Weil, J., Soucacos, P., & Webb, S. (2017a). *Dispersion modeling guidance for airports addressing local air quality concerns*. Transportation Research Board Airport Cooperative Research Program (ACRP) Research Report 179. http://nap.edu/24881

Arunachalam, S., V. Isakov, T. Barzyk, A. Venkatram, J. Weil, B. Naess, A. Valencia, C. Seppanen, J. Brandmeyer (2017b). C-AIRPORT: A New Web-based Air Quality Model for Community-Scale Assessments around Airports, *In Proceedings of the 18th International Conference on Harmonisation within Atmospheric Dispersion Modelling for Regulatory Purposes*, Bologna, Italy, October 2017.

Arunachalam, S., B. Naess, C. Seppanen, A. Valencia, J. Brandmeyer, A. Venkatram, J. Weil, V. Isakov, T. Barzyk *(2019).* A new bottom-up emissions estimation approach for aircraft sources in support of air quality modeling for community-scale assessments around airports, *International J. Environ. Pollution*, 65(123):43 - 58, (2019). https://doi.org/10.1504/IJEP.2019.101832.

Barrett, S. R. H., Britter, R. E., & Waitz, I. A. (2013). Impact of aircraft plume dynamics on airport local air quality. *Atmospheric Environment, 74*, 247–258. doi:10.1016/j.atmosenv.2013.03.061

Barzyk, T.M., V. Isakov, S. Arunachalam, A. Venkatram, R. Cook, B. Naess (**2015**). A Near-Road Modeling System for Community-Scale Assessments of Mobile-Source Air Toxics: The Community Line Source (C-LINE) Modeling System, *Environ. Model. Software,* 66:46-56.

Briggs, G. A. (1965). A plume rise model compared with observations. *Journal of Air Pollution Control Association, 15*, 433–438. doi:10.1080/00022470.1965.10468404

Carslaw, D., Beevers, S., Ropkins, K., Bell, M., 2006. Detecting and quantifying aircraft and other on-airport contributions to ambient nitrogen oxides in the vicinity of a large international airport. Atmos. Environ. 40, 5424–5434. doi:10.1016/j.atmosenv.2006.04.062

Chowdhury, B.; Karamchandani, P.; Sykes, R.; Henn, D.; Knipping, E. Reactive puff model SCICHEM: Model enhancement and performance studies. Atmos. Environ. 2015, 117, 242−258.

Cimorelli, A. J., Perry, S. G., Venkatram, A., Weil, J., Paine, R., Wilson, R. B., Lee, R. F., Peters, E. D., & Brode, R. W. (2005). AERMOD: A dispersion model for industrial source applications. Part I: general model formulation and boundary layer characterization. *Journal of Applied Meteorology 44*, 682–693.

Cole, H. S., & Summerhays, J. E. (1979). A Review of Techniques Available for Estimating Short-Term NO_2 concentrations. *Journal of the Air Pollution Control Association*, *29*(8), 812–817. https://doi.org/10.1080/00022470.1979.10470866

Cox, W. M., & Tikvart, J. A. (1990). A statistical procedure for determining the best performing air quality simulation model. *Atmos. Environ. Part A, Gen. Top. 24*, 2387–2395.

Federal Aviation Administration. (2014). *Aviation environmental design tool (AEDT).* https://aedt.faa.gov/

Huang, J., P. Vennam, F.S. Binkowski, B. Murphy and S. Arunachalam (2017). A Nationwide Assessment of Particle Number Concentrations from Commercial Aircraft Emissions in the U.S., *Presented at the 36th Annual Conference of the American Association for Aerosol Research*, Raleigh, NC, October 2017.

Jiang, W., S. Smyth, É. Giroux, H. Roth, and D. Yin, "Differences between CMAQ fine mode particle and PM2.5 concentrations and their impact on model performance evaluation in the lower Fraser valley," Atmos. Environ., vol. 40, no. 26 (2006) : 4973–4985.

Kim, B., J. Rachami, D. Robinson, B. Robinette, K. Nakada, S. Arunachalam, N. Davis, B.H. Baek. U. Shankar, K. Talgo, D. Yang, A. Hanna, R. Wayson, G. Noel, S.S. Cliff, Y. Zhao, P. Hope and P. Kumar (2012). "Guidance for Quantifying the Contribution of Airport Emissions to Local Air Quality", Transportation Research Board Airport Cooperative Research Program (ACRP) Report 71, Washington, D.C. Available at: http://onlinepubs.trb.org/onlinepubs/acrp/acrp_rpt_071.pdf

Martin, A. (2006). *Verification of FAA's emissions and dispersion modeling system (EDMS).* University of Central Florida, Orlando, Florida.

Meng, Z. and J. H. Seinfeld, "On the Source of the Submicrometer Droplet Mode of Urban and Regional Aerosols," Aerosol Sci. Technol., vol. 20, no. 3 (1994): 253–265.

Murphy, B.; F.S. Binkowski; E. WInijkul; T. Olenius; M. Alvarado; I. Rippinen; M. Woody and H.O.T. Pye (2017). Quantifying Primary and Secondary Ultrafine Particle Contributions in the U.S. with CMAQ-NPF, *Presented at the 36th Annual Conference of the American Association of Aerosol Research*, Raleigh, NC, October 2017.

Rienecker, M. M.; Suarez, M. J.; Gelaro, R.; Todling, R.; Bacmeister, J.; Liu, E.; Bosilovich, M. G.; Schubert, S. D.; Takacs, L.; Kim, G. K.; et al. MERRA: NASA's modern-era retrospective analysis for research and applications. *J. Clim.* **2011**, *24* (14), 3624–3648.

Tetra Tech, Inc. (2013). *LAX air quality and source apportionment study*, Los Angeles World Airports.

Tetra Tech, Inc., 2013. LAX Air Quality and Source Apportionment Study. Los Angeles World Airports. Available at: http://www.lawa.org/airQualityStudy.aspx?id=7716.

Valencia, A., S. Arunachalam, D. Heist, D. Carruthers, and A. Venkatram (**2018**). Development and Evaluation of the R-LINE Model Algorithms to Account for Chemical Transformation in the Near-road Environment, *Transp. Res. Part D: Transp. Environ.,* 59, 464 – 477.

Venkatram, A., Karamchandani, P., Pai, P., Goldstein, R., 1994. The development and application of a simplified ozone modeling system (SOMS). *Atmos. Environ.* 28(22), 3665–3678. http://dx.doi.org/10.1016/1352-2310(94)00190-V .

Venkatram, A., Karamchandani, P., Pai, P., Sloane, C., Saxena, P., & Goldstein, R. (1997). The Development of a Model to Examine Source-Receptor Relationships for Visibility on the Colorado Plateau. *Journal of the Air & Waste Management Association*, *47*(3), 286–301. https://doi.org/10.1080/10473289.1997.10464453

Wayson, R. L., Fleming, G. G., & Iovinelli, R. (2009). Methodology to estimate particulate matter emissions from certified commercial aircraft engines. *Journal of the Air & Waste Management Association, 59(1)*, 91–100. https://doi.10.3155/1047-3289.59.1.91

Wayson, R.L., Fleming, G.G., Kim, B., Eberhard, W.L., Brewer, W.A., 2004. Final report: the use of LIDAR to characterize aircraft initial plume characteristics (No. FAA-AEE-04-01; DTS-34-FA34T-LR3;). FAA.

Wilkerson, J. T.; Jacobson, M. Z.; Malwitz, A.; Balasubramanian, S.; Wayson, R.; Fleming, G.; Naiman, A. D.; Lele, S. K. Analysis of emission data from global commercial aviation: 2004 and 2006. *Atmos. Chem. Phys.* **2010**, *10*, 6391–6408.

Yamartino, R. J., & Donald M. R. (1979). Updated model assessment of pollution at major U.S. airports. *Journal of the Air Pollution Control Association, 29(2)*, 128–132. https://doi.10.1080/00022470.1979.10470767

Appendix A: Exceedance Computation Using CMAQ Results

$PM_{2.5}$ (Jan)	Base-NEI	No-Airport	Base-NEI - No-Airport
25 µg/m³	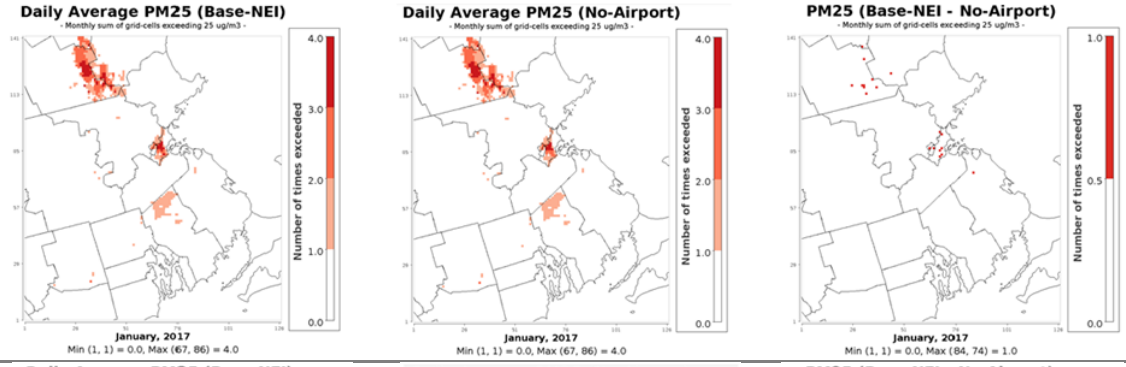		
30 µg/m³	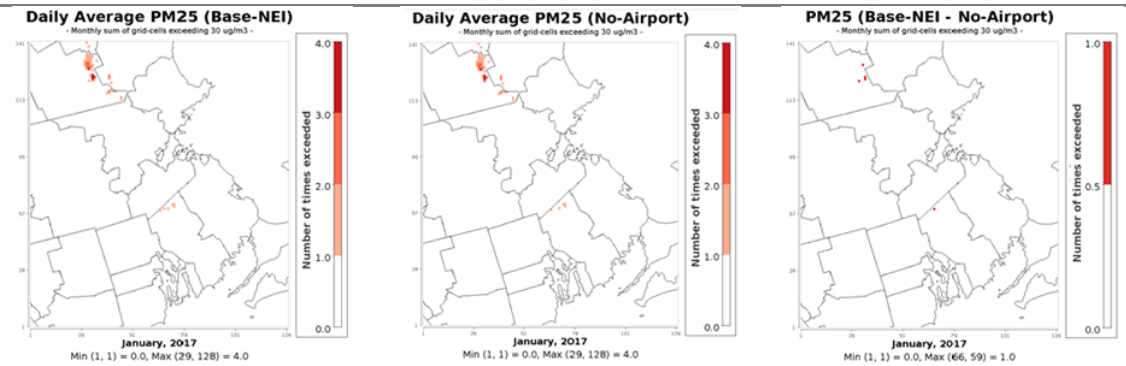		
35 µg/m³	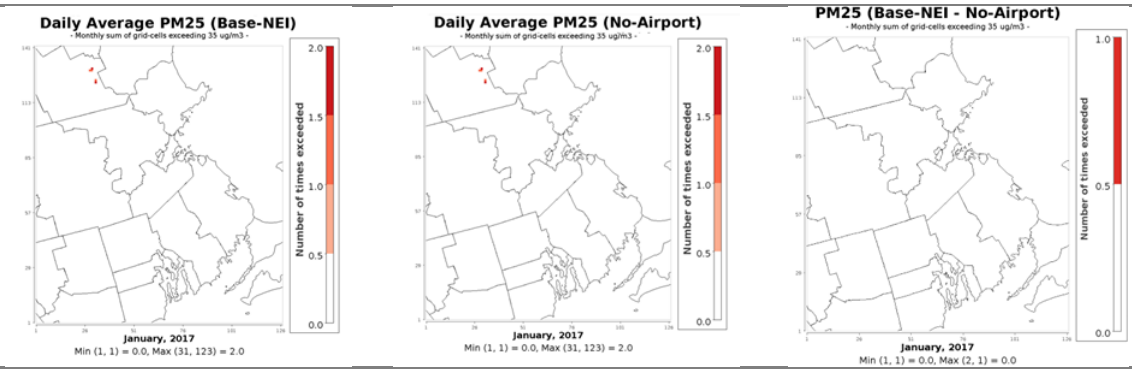		

Figure A1. Comparing daily $PM_{2.5}$ sum by concentration (25-35 µg/m³) at all grid-cells for January.

$PM_{2.5}$ Annual	Base-NEI	No-Airport	Base-NEI - No-Airport
8 µg/m³	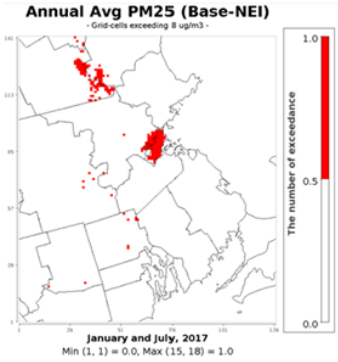	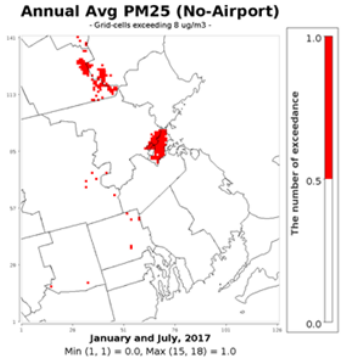	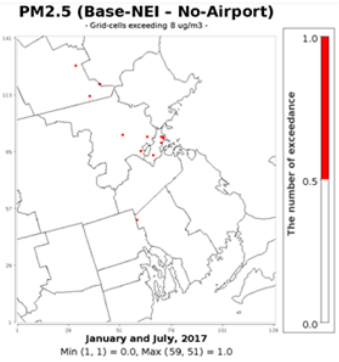
10 µg/m³	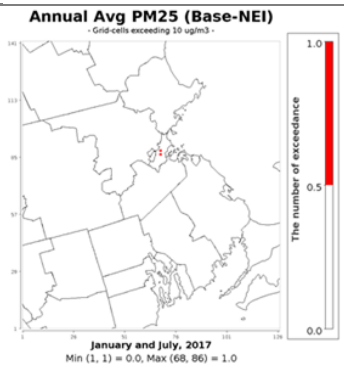	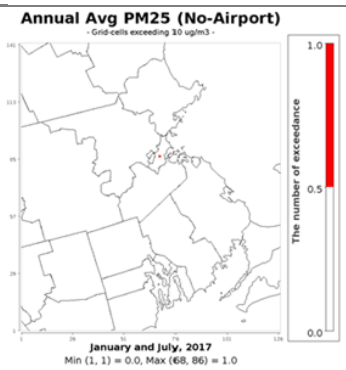	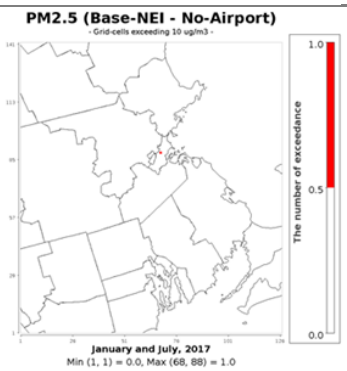

Figure A2. Comparing annual $PM_{2.5}$ average (January + July average) by concentration (8-10 µg/m³) at all grid-cells.

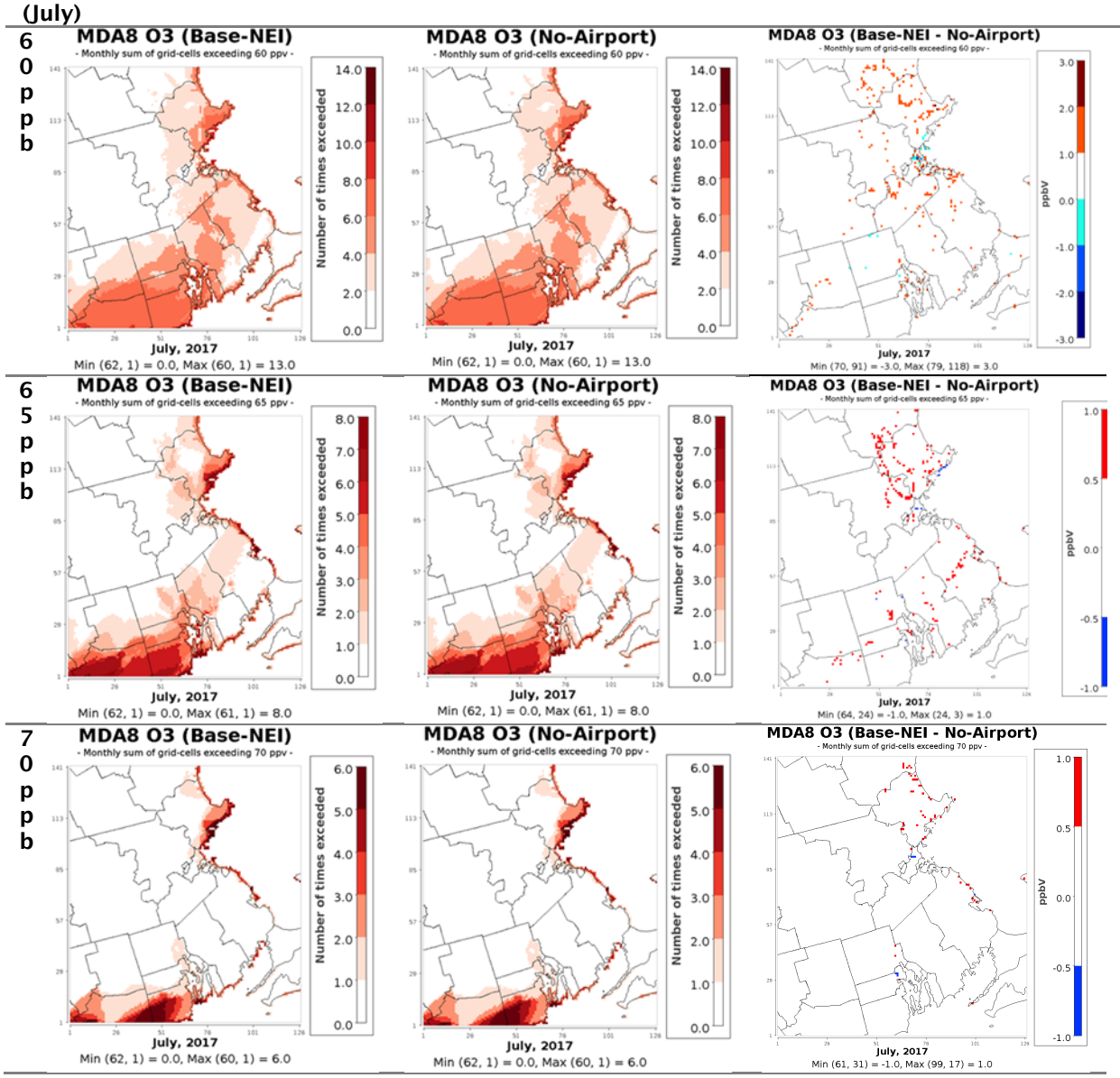

Figure A3. Comparing maximum daily average 8-hour O_3 each day by concentration (60-70 ppb) at land grid-cells for July.

Table A1. Summary of issues related to AEDT data for BOS airport study.

Color code for data availability according to the user-manual and BU's PDARS data

Available in BU's data or optional information	Can be created from BU's data or a recommended option	Can't be created from BU's data

Color code for data importance:

Recommended	Required

Data availability for aircraft operation csv input file columns (needed unless specified in Comments column):

Column Name	Description	Notes	Data Availability	Comments
AirOp_UserID	User-defined operation ID		Can be created from BU's data	Required. Input file requirements by operation type for schedule-based operations
AcType	ICAO/IATA aircraft type (used to map aircraft types to an engine) e.g., B738	Can be found in AEDT equipment tab, Equipment: Aircraft data grid, Airframe Model column	Can be created from BU's data and Appendix (shared by BU)	Required
AirframeModel	Airframe model name e.g., Boeing 737-800 Series	Can be found in AEDT equipment tab	Can be created from BU's data and Appendix (shared by BU)	Required
EngineCode	Engine ID, e.g., 203	Can be found in AEDT equipment tab	Can be created from BU's data and Appendix (shared by BU)	Required
EquipID	Equipment ID	Can be found in AEDT equipment tab	Can't be created from BU's data	Not needed if we have data for either of the combinations of AirframeModel and EngineCode or AcType and EngineCode
OpType	Operation type (A) Arrival, (D) Departure, (T) Touch and Go, (F) Circuit, (V) Overflight, (5) Runway to Runway (great circle)		Can't be created from BU's data	Required
OpCount	Operation count	This value can represent an average annual day, distinct operation count (i.e., 1), or annual number of operations	Can't be created from BU's data	Required
OpTime	Operation time	e.g., 2010-01-06 08:24:00.000	Can be created from BU's data	Required

DepApt	Departure airport ICAO code	Can be found in the Airports tab, Add Existing Airport dialog	Can be created from BU's data	Required for departures
ArrApt	Arrival airport ICAO code	Can be found in the Airports tab, Add Existing Airport dialog	Can be created from BU's data	Required for arrivals
DepRwyEnd Name	Departure runway end name e.g., 10L	This runway end must exist in the study prior to importing	Can't be created from BU's data	Required for departures
ArrRwyEnd Name	Arrival runway end name e.g., 10L	This runway end must exist in the study prior to importing	Can't be created from BU's data	Required for arrivals
ProfileID	Aircraft's profile ID e.g., 253	If not provided, the Profile Name will be used in conjunction with the stage length to determine the profile	Can't be created from BU's data	Optional
ProfileName	Name of flight performance profile e.g., STANDARD, ICAO_A, ICAO_B	If both the profile ID and profile name are unspecified, STANDARD is assumed	Can't be created from BU's data	Recommended
TrackName	Track name from the tracks input file or an existing track name	Track name is option for operational profile-based operations.	Can't be created from BU's data	Optional
StageLength	Stage length 1-9 or M		Can't be created from BU's data	Recommended
TaxiOut_Sec	Taxi-out time in seconds		Can't be created from BU's data	Optional
TaxiIn_Sec	Taxi-in time in seconds		Can't be created from BU's data	Optional
ArrGatrName	Arrival gate name	This gate must exist in the study prior to importing	Can't be created from BU's data	Required
QuarterHourly ProfileName	Name of quarter-hourly operational profile	Used to define a profile-based operation When defining profile-based operations, all three profile types must be defined (quarter hour, daily, and monthly) and the operational profiles must exist in the study prior to importing	Can't be created from BU's data	Required for Profile-based operations
DailyProfile Name	Name of daily operational profile	Used to define a profile-based operation When defining profile-based operations, all three profile types must be defined (quarter hour, daily, and monthly) and the operational profiles must exist in the study prior to importing	Can't be created from BU's data	Required for Profile-based operations

MonthlyProfile Name	Name of daily operational profile	Used to define a profile-based operation When defining profile-based operations, all three profile types must be defined (quarter hour, daily, and monthly) and the operational profiles must exist in the study prior to importing	Can't be created from BU's data	Required for profile-based operations

Data availability for tracks csv input file columns (needed):

Column Name	Description	Notes	Data Availability	Comments
APT_CODE	Airport Code		Can be created	Required
RWY_END_NAME	Runway end name	Runway end must exist in the study prior to importing. Not required for overflight tracks	Can be created	Required
TRACK_NAME	Track name	Track names in the study must be unique	Can be created	Required
TRACK_TYPE	Track type		Can be created	Required
OP_TYPE	Operation type		Can't be created from BU's data	Required
RUNWAY_END_DELTA_ DISTANCE	Delta distance from nominal start-roll or touch down point	Typically set to 0	Can be created	Required
AIRCRAFT_TYPE	0 for fixed wing, 1 for helicopter		Can be created from BU's data	Required
VECTOR_COURSE_AT_ HELIPAD	Direction for helicopter operations		Can't be created from BU's data	Required
SUBTRRACK_NUM	Sub-track number		Can't be created from BU's data	Required
PCT_DISPERSION	Percent of flights dispersed to the sub-track		Can't be created from BU's data	Required
SEGMENT_NUM	Number of the current segment		Can't be created from BU's data	Required
SEGMENT_TYPE	Segment type		Can't be created from BU's data	Required
PARAM_1	Point-type track: latitude (in deg) Vector-type track: angle in distance/radius (in feet)		Can be created from BU's data	Required
PARAM_2	Point-type track: longitude (in deg) Vector-type track: angle in distance/radius (in feet)		Can be created from BU's data	Required